Diagnosing ocean feedbacks to the MJO: SST-modulated surface fluxes and the moist static energy budget

AGU PUBLICATIONS

JGR

Journal of Geophysical Research: Atmospheres

RESEARCH ARTICLE
10.1002/2016JD025098

Key Points:
- SST variations reduce wind-driven fluxes
- SST offset of wind-driven flux maximizes in the subtropics
- SST fluctuations support on-equator convection and MJO propagation

Correspondence to:
C. A. DeMott,
demott@atmos.colostate.edu

Citation:
DeMott, C. A., J. J. Benedict, N. P. Klingaman, S. J. Woolnough, and D. A. Randall (2016), Diagnosing ocean feedbacks to the MJO: SST-modulated surface fluxes and the moist static energy budget, *J. Geophys. Res. Atmos.*, *121*, 8350–8373, doi:10.1002/2016JD025098.

Received 15 MAR 2016
Accepted 30 JUN 2016
Accepted article online 7 JUL 2016
Published online 28 JUL 2016

Diagnosing ocean feedbacks to the MJO: SST-modulated surface fluxes and the moist static energy budget

Charlotte A. DeMott[1], James J. Benedict[2], Nicholas P. Klingaman[3], Steven J. Woolnough[3], and David A. Randall[1]

[1]Department of Atmospheric Science, Colorado State University, Fort Collins, Colorado, USA, [2]Rosenstiel School of Marine and Atmospheric Science, University of Miami, Miami, Florida, USA, [3]National Centre for Atmospheric Science and Department of Meteorology, University of Reading, Reading, UK

Abstract The composite effect of intraseasonal sea surface temperature (SST) variability on the Madden-Julian Oscillation (MJO) is studied in the context of the column-integrated moist static energy ($\langle m \rangle$) budget using data from the European Centre for Medium-Range Weather Forecasts Interim Reanalysis (ERA-I). SST fluctuations influence the Δq and ΔT parts of the bulk surface latent and sensible heat flux calculations, respectively, each of which influence column $\langle m \rangle$. Reynolds decomposition of latent and sensible heat fluxes (LH and SH) reveal that the thermodynamic perturbations (e.g., $\Delta q' \overline{|\mathbf{V}|}$ for LH) modestly offset the equatorial wind-driven perturbations ($\overline{\Delta q}|\mathbf{V}|'$) and $\langle m \rangle$, but strongly offset the subtropical $\overline{\Delta q}|\mathbf{V}|'$ and $\langle m \rangle$. Column moistening east of MJO convection is opposed by $\overline{\Delta q}|\mathbf{V}|'$ and supported by $\Delta q' \overline{|\mathbf{V}|}$. Impacts of intraseasonal SST fluctuations are analyzed by recomputing surface flux component terms using 61 day running-mean SST. Differences between "full SST" and "smoothed SST" projections onto $\langle m \rangle$ and its tendency ($\partial \langle m \rangle / \partial t$) yield the "SST effect" on the MJO $\langle m \rangle$ budget. Particularly in the Indian Ocean, intraseasonal SST fluctuations maintain equatorial $\langle m \rangle$ anomalies at a rate of 1%–2% d^{-1} and damp subtropical $\langle m \rangle$ anomalies at a similar rate. Vertical advection ($-\langle \omega \partial m / \partial p \rangle$) exports 10%–20% of $\langle m \rangle$ per day, implying that the SST modulation of surface fluxes offsets roughly 10% of equatorial $\langle m \rangle$ export and amplifies by 10% the subtropical $\langle m \rangle$ export by $-\langle \omega \partial m / \partial p \rangle$. SST fluctuations support MJO propagation by encouraging on-equator convection and the circulation anomalies that drive MJO propagation, and by contributing up to 10% of $\partial \langle m \rangle / \partial t$ across the Warm Pool.

1. Introduction

The Madden-Julian Oscillation (MJO) is a tropical large-scale (~18,000 km) disturbance that propagates east with a period of 30–70 days [*Madden and Julian*, 1971, 1972]. The MJO convective signal is most prominent over the warm waters of the Indian and West Pacific Oceans where it propagates east at about 5 m s^{-1}. MJO convective heating forces an equatorially trapped first baroclinic circulation response (zonal wave number $k \approx 1$) whose upper level wind anomaly travels around the globe, speeding up near the dateline as it becomes decoupled from convection. The large-scale, slow-moving heating source of the MJO can perturb the height and wind fields beyond the tropics, driving teleconnection responses that can affect weather across the globe (see *Zhang* [2013] for a full description).

The spatially large (4000–8000 km zonally) envelope of MJO convection encapsulates individual convective disturbances associated with a variety of equatorially trapped wave types, such as Kelvin, equatorial Rossby, mixed-Rossby gravity (i.e., Yanai), and eastward and westward inertia gravity waves [*Dias et al.*, 2013]. The circulation anomalies excited by the integrated heating of MJO convection resemble low wave number Kelvin waves to the east and equatorial Rossby waves to the west of MJO convection [e.g., *Gill*, 1980; *Wang*, 1988; *Roundy*, 2012]. Large-scale measures of MJO activity, however, such as convection, rainfall, and wind anomalies, do not project onto equatorial wave modes [*Wheeler and Kiladis*, 1999], implying that the fundamental controls of MJO behavior cannot be understood within the theoretical framework of these modes. Instead, a large body of evidence points to the central role of column moisture in regulating the observed characteristics of MJO convection [e.g., *Bladé and Hartmann*, 1993; *Hu and Randall*, 1994; *Kemball-Cook and Weare*, 2001; *Tian et al.*, 2006; *Benedict and Randall*, 2007; *Thayer-Calder and Randall*, 2009]. Specifically, a gradual buildup of column moisture is observed prior to development of MJO convection. Once an MJO event is established, column moistening to the east and drying to the west of the convective envelope promotes eastward propagation of convection and its associated circulation anomalies.

The weight of evidence based on decades of study holds that the MJO is primarily driven by atmospheric processes. This paradigm is supported by several lines of evidence: theory and simple models [e.g., *Gill*, 1980; *Lau and Peng*, 1987; *Wang and Rui*, 1990, 1994; *Majda and Stechmann*, 2009, 2011] can describe the gross features of the MJO without considering time-varying ocean processes or their feedbacks to the atmosphere; the ability of general circulation models to simulate the MJO is closely linked to their ability to reproduce the observed relationship of rainfall and vertical profiles of relative humidity [*Thayer-Calder and Randall*, 2009; *Kim et al.*, 2009], even in uncoupled simulations [e.g., *Benedict and Randall*, 2009; *Klingaman and Woolnough*, 2014a]; and moist static energy budgets of the MJO point to the dominant roles of longwave heating and moisture advection to MJO maintenance and propagation, respectively [*Maloney*, 2009; *Kiranmayi and Maloney*, 2011; *Andersen and Kuang*, 2012; *Kim et al.*, 2014; *Chikira*, 2014; *Arnold and Randall*, 2015].

On the other hand, there is also evidence to suggest nonnegligible ocean feedbacks to the MJO. Observations of MJO convection over the Maritime Continent region reveal distinctly more intraseasonal variability over the ocean than the islands [*Sobel et al.*, 2010]. Numerous modeling studies demonstrate improvements in MJO simulation and/or forecasts when atmosphere-only models are coupled to ocean models (see *DeMott et al.* [2015] for a summary). Improvements gained by air-sea coupling, however, are not consistent across models: ocean coupling can alter MJO phase speed [e.g., *Maloney and Sobel*, 2004; *Marshall et al.*, 2008; *Wang and Seo*, 2009]; it can promote eastward propagation in cases where it is weak or nonexistent [e.g., *Inness and Slingo*, 2003; *Klingaman and Woolnough*, 2014b]; it can encourage propagation beyond the Indian Ocean when the atmosphere-only model cannot [e.g., *Kemball-Cook et al.*, 2002]. The variety of responses to coupling across models poses a challenge to understanding the processes through which ocean feedbacks influence the MJO. Additionally, studies comparing the MJO in coupled and uncoupled simulations of the same model often include mean state differences between the two simulations, since SST biases often develop in the coupled run. The strong sensitivity of the simulated MJO to the mean state [*Slingo et al.*, 1996; *Zhang et al.*, 2006; *Klingaman and Woolnough*, 2014b] complicates the analysis of ocean feedbacks in such studies.

SST variations on intraseasonal time scales are a complicated function of atmospheric fluxes of heat, momentum, and fresh water to the ocean surface and the ocean response to those fluxes [*DeMott et al.*, 2015, and references therein]. Results from the international Cooperative Indian Ocean Experiment on Intraseasonal Variability in Year 2011 (CINDY)/Dynamics of the Madden-Julian Oscillation (DYNAMO) [*Yoneyama et al.*, 2013] highlighted differences in the magnitudes of SST anomalies that exist among MJO events [*Gottschalck et al.*, 2013; *de Szoeke et al.*, 2015] and the impacts of those SST anomalies on MJO predictions [e.g., *Shinoda et al.*, 2013; *Wang et al.*, 2015; *Fu et al.*, 2015]. Factors that favor strong positive SST anomalies within the MJO life cycle include a period of strongly suppressed convection and calm winds such that intense solar heating, reduced surface fluxes from the ocean, and suppressed wind mixing of the upper ocean concentrates input energy in the upper few meters of the ocean. These processes lead to a shoaling, or thinning, of the ocean mixed layer (the well-mixed surface layer that is analogous to the atmospheric boundary layer). Strong negative SST anomalies are a consequence of reduced solar heating due to enhanced cloudiness and strong winds that cool the upper ocean via surface fluxes and vertical mixing, ocean upwelling, and/or advection of cold upper ocean waters [e.g., *Weller and Anderson*, 1996; *Lau and Sui*, 1997; *Hendon and Glick*, 1997; *Duvel et al.*, 2004; *Halkides et al.*, 2015].

SST anomalies driven by MJO forcing can directly alter surface fluxes of latent and sensible heat through their effects on vertical gradients of near-surface specific humidity and temperature, respectively. Upwelling infrared surface fluxes are also affected. For a given wind speed and relative humidity, a 1 K increase in SST increases latent and sensible heat fluxes by approximately 18 W m^{-2} ($\sim$16%) and 2.5 W m^{-2} ($\sim$23%), respectively, while upwelling longwave fluxes increase by about 6 W m^{-2} ($\sim$1%) [*Webster et al.*, 1996].

Intraseasonal SST-modulated surface fluxes are hypothesized to influence the atmosphere through a variety of processes. First, wind-driven surface fluxes in the vicinity of MJO convection can directly energize and moisten the atmosphere, providing a positive feedback to maintain MJO convection. This process is sometimes referred to as the wind-evaporative-SST feedback [*Neelin et al.*, 1987; *Xie and Carton*, 2004; *Lin et al.*, 2008] or, for historical reasons, the modified wind-induced surface heat exchange ("modified WISHE" [*Maloney and Sobel*, 2004]) mechanism, since it incorporates the WISHE mechanism first described by *Emanuel* [1987] and *Neelin et al.* [1987]. The modification of the original WISHE paradigm refers to the relaxation of the assumption of mean low-level easterlies over the Warm Pool, since the observed mean state exhibits low-level westerlies. Second, SST-enhanced surface fluxes on one side of a sharp SST gradient can induce a hydrostatic reduction of surface pressure and a wind adjustment that drives enhanced boundary layer convergence on the warm side of the gradient [*Lindzen and Nigam*, 1987; *Back and Bretherton*, 2009; *Hsu and Li*, 2012; *Li and Carbone*, 2012]. Third, quiescent conditions during the MJO suppressed phase can produce a thin stratified surface layer during daylight and a large diurnal SST response to solar forcing [*Bellenger and Duvel*, 2009; *Bellenger et al.*, 2010; *Matthews et al.*, 2014]. During CINDY/DYNAMO, diurnal SST ranges of 1–3 K were observed to dramatically increase diurnal surface turbulent fluxes, initiating trade cumulus convection that moistened the lower atmosphere as the MJO transitioned from suppressed to active phases [*Ruppert and Johnson*, 2015].

Assessing which of these feedbacks are important to the MJO is difficult, since the *direct* effects of SST-induced changes to surface fluxes can promote secondary, or *indirect*, changes to processes not directly related to surface fluxes but of known importance to MJO dynamics. Such processes include cloud radiative feedbacks, diabatic heating, and moisture advection. The complex response of the MJO to SST perturbations makes it difficult to diagnose the net effects of ocean feedbacks.

Nevertheless, all potential ocean feedbacks to the MJO are rooted in modifications of surface fluxes by SST variations. It follows that understanding the impact of SST perturbations on surface fluxes within the MJO life cycle is a first step toward understanding the processes through which the ocean impacts the MJO. We present a diagnostic approach for studying the direct effects of SST variations within the framework of the MJO moist static energy (MSE) budget using a data record of comparable length to those generated by free running climate simulations. Our paper is organized as follows: section 2 discusses the data used in this study, methods for assessing SST-modulated surface fluxes, and a method to assess SST impacts within the MSE budget framework. Section 3 presents the results of our analysis, including maps of the mean state and intraseasonal standard deviation of flux-related variables, how these variables and MSE budget source terms vary across the MJO life cycle, and contributions of SST fluctuations to $\langle m \rangle$ maintenance and tendency. Interpretation of the results and a discussion of their utility for diagnosing atmosphere-ocean feedbacks in models are given in section 4. Our findings are summarized in section 5.

2. Data and Methods

2.1. Data

We use 1986–2013 daily mean data from the European Centre for Medium Range Weather Forecasts (ECMWF) Interim Reanalysis (ERA-I) [*Dee et al.*, 2011] to assess the role of SST variations on the MJO. ERA-I data are available as early as 1979, but we limit our analysis to periods after 1986 when satellite SST estimates in the tropical Pacific are better constrained by in situ buoy measurements [*Reynolds et al.*, 2002]. The reanalysis provides consistent atmospheric data over a sufficiently long period that are well suited to MSE budget studies.

The SST observations used to produce ERA-I are not consistent throughout our analysis period. Prior to the 2002 introduction of daily mean SST into the assimilation, only weekly mean SST was used [*Dee et al.*, 2011]. Including the years with weekly SST in our analysis likely underestimates the SST impact on the MJO, whereas including only those years where daily SST were used would reduce our sample size. Second, reanalysis surface fluxes are estimated based on input winds and surface air temperature and humidity, which themselves may contain errors that introduce potentially important biases in the flux [e.g., *Chaudhuri et al.*, 2013; *Kent et al.*, 2013; *Brown and Kummerow*, 2014; *Valdivieso et al.*, 2015]. Finally, reanalysis systems employ time step "analysis increment" corrections so that prognostic model fields do not drift too quickly from input observations [*Dee et al.*, 2011]. These analysis increments contribute to the MSE budget residual (section 2.3), which is nearly as large as its tendency, $\partial\langle m \rangle/\partial t$, for ERA-I [*Kiranmayi and Maloney*, 2011]).

2.2. Surface Flux Decomposition

Our assessment of SST perturbations within the MSE budget begins with the bulk flux formulae for surface latent and sensible heat [*Fairall et al.*, 1996]:

$$\mathrm{LH} = \rho L_v C_e |\mathbf{V}| \Delta q; \quad \Delta q = q^*_{\mathrm{SST}} - q_{\mathrm{air}} \tag{1}$$

$$\mathrm{SH} = \rho C_p C_h |\mathbf{V}| \Delta T; \quad \Delta T = \mathrm{SST} - T_{\mathrm{air}} \tag{2}$$

Table 1. Fractional SST Effect on Wind-Driven Flux Perturbations and Total Anomaly Surface Fluxes Averaged 10°S–10°N for the Indian and West Pacific Oceans[a]

x	Indian Ocean (50°E–90°E)	West Pacific (120°E–170°E)
$\overline{\Delta q}\|\mathbf{V}\|'$	−0.09	−0.07
$\overline{\Delta T}\|\mathbf{V}\|'$	−0.33	−0.14
LH	0.03	0.00
SH	0.23	0.14

[a]Values shown are $F_x(E_{LH})$ and $F_x(E_{SH})$, calculated as in equation (6), where $E_{LH} = LH^*_{SST} - LH^*_{\overline{SST}}$ and $E_{SH} = SH^*_{SST} - SH|^*_{\overline{SST}}$.

where ρ is air density, L_v is the latent heat of vaporization, C_e is the transfer coefficient for latent heat, $|\mathbf{V}|$ is the near-surface wind speed, q^*_{SST} is the saturation specific humidity at T = SST, and T_{air} and q_{air} are temperature and specific humidity, respectively, at ~2 m above the surface. Relative contributions of wind and Δq fluctuations to the latent heat flux anomalies are estimated with the aid of Reynolds decomposition:

$$LH^* = \rho L_v C_e (\underbrace{\overline{\Delta q}|\mathbf{V}|'}_{\text{wind-driven}} + \underbrace{\Delta q' \overline{|\mathbf{V}|}}_{\text{thermodynamic}} + \underbrace{\Delta q'|\mathbf{V}|'}_{\text{second order}}) \tag{3}$$

where quantities with overbars represent slowly varying background quantities (calculated as the 61 day running mean of the total field), and primed quantities represent departures from the background state. The sensible heat flux is decomposed in a similar manner. Hereafter, primed notation is retained only within surface flux component terms (e.g., $\overline{\Delta q}|\mathbf{V}|'$) but not for anomalies of single variable (e.g., LH′ is written as LH). Flux anomalies estimated as in equation (3) are denoted as LH* and SH* to distinguish them from LH and SH. The terms on the right-hand side describe the wind-driven, thermodynamic, and second-order perturbations to the flux, respectively. At each grid point, the terms in parentheses in equation (3) are calculated using reanalysis fields, including SST (i.e., skin temperature) to compute Δq, and their sums are regressed onto LH at the corresponding grid point to estimate the scaling factor that corresponds to $\rho L_v C_e$. Offline calculations using buoy data (not shown) indicate that this approximation results in root-mean-square errors <5% across the Warm Pool and correlation coefficient $r \approx 0.98$ for LH and LH*. The same procedure for SH* yields similar accuracy. The impact of SST variations on surface fluxes is then estimated by recalculating equation (3) but using a 61 day running-mean SST time series in equations (1) and (2). The difference between the LH* and SH* using the unsmoothed (i.e., "full") and smoothed SST represents the effect of intraseasonal SST variations on the fluxes. Evaluations of equation (3) using the full SST are written as, for example, LH^*_{SST} and SH^*_{SST}, while evaluations using the smoothed SST are written as $LH^*_{\overline{SST}}$ and $SH^*_{\overline{SST}}$.

The SST modulation of surface fluxes in the context of the MJO has been studied extensively [e.g., *Krishnamurti et al.*, 1988; *Hendon and Glick*, 1997; *Shinoda et al.*, 1998; *Maloney and Esbensen*, 2007; *Araligidad and Maloney*, 2008; *DeMott et al.*, 2015; *Riley Dellaripa and Maloney*, 2015]. Figure 1 illustrates the subtle effects of SST perturbations on LH* for a point in the Indian Ocean. Blue solid and dashed curves in Figure 1a represent $\Delta q'\overline{|\mathbf{V}|}_{SST}$ and $\Delta q'\overline{|\mathbf{V}|}_{\overline{SST}}$. Compared to $\Delta q'\overline{|\mathbf{V}|}_{SST}$, the $\Delta q'\overline{|\mathbf{V}|}_{\overline{SST}}$ amplitude is reduced and its phase is shifted toward more negative lags. The $\Delta q'\overline{|\mathbf{V}|}$ curves in Figure 1a offset $\overline{\Delta q}|\mathbf{V}|'$ (red curve), so that the resulting LH* amplitudes are slightly less than the $\overline{\Delta q}|\mathbf{V}|'$ amplitude (Figure 1b, purple curves). Compared to $\Delta q'\overline{|\mathbf{V}|}_{\overline{SST}}$, the different phasing and larger amplitude of $\Delta q'\overline{|\mathbf{V}|}_{SST}$ results in a greater reduction in LH^*_{SST} amplitude *and* a greater phase shift of LH^*_{SST} toward negative lags. An important consequence of the $\Delta q'\overline{|\mathbf{V}|}_{SST}$-driven phase shift is the slight enhancement of LH^*_{SST} over $LH^*_{\overline{SST}}$ at day 0, which corresponds to maximum MJO convection. Table 1 summarizes the SST-driven offset of $\overline{\Delta q}|\mathbf{V}|'$ and the day 0 enhancement of LH^*_{SST} over $LH^*_{\overline{SST}}$ averaged over the tropical Indian and West Pacific Oceans. Reductions of wind-driven perturbations of latent and sensible heat fluxes by SST variability are larger over the Indian Ocean (9% and 33%) than over the West Pacific (7% and 14%). SST-driven enhancement of LH* and SH* is also larger in the Indian Ocean (3% and 23%) than in the West Pacific (0% and 14%). We attribute these differences to more intense ocean cooling in the Indian Ocean due to the shallower ocean mixed layer and thermocline.

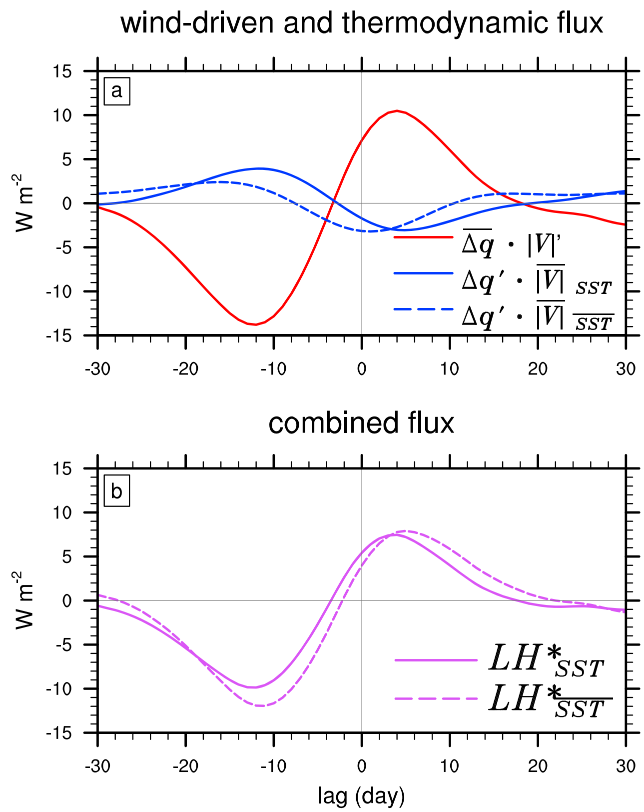

Figure 1. (a) Lagged regression of $\overline{\Delta q}|\mathbf{V}|'$ (red), $\Delta q'\overline{|\mathbf{V}|}_{SST}$ (solid blue), and $\Delta q'\overline{|\mathbf{V}|}_{\overline{SST}}$ (dashed blue) onto 20–100 day filtered $\langle m \rangle$ averaged over the central Indian Ocean (10°S–10°N; 65°E–75°E). (b) LH^*_{SST} (solid magenta) and $LH^*_{\overline{SST}}$ (dashed magenta) as defined in equation (3) for the same averaging area.

2.3. The Moist Static Energy Budget

Analysis of the vertically integrated MSE, $\langle m \rangle$, budget provides insight into the mechanisms that regulate MJO convection. The vertically integrated moist static energy, $\langle m \rangle$ is defined as

$$\langle m \rangle = \langle c_p T \rangle + \langle gZ \rangle + \langle L_v q \rangle - \langle L_f q_i \rangle \tag{4}$$

where c_p is the specific heat of air at constant pressure, T is temperature, g is the gravitational constant, Z is height, q and q_i are the specific quantities of water vapor and ice, respectively, and L_v and L_f are the latent heats of vaporization and fusion, respectively. Angled brackets represent vertical integration from 1000–100 hPa. The tendency of $\langle m \rangle$ is described by processes that moisten or heat the column:

$$\partial \langle m \rangle / \partial t = -\langle \mathbf{V} \cdot \nabla m \rangle - \langle \omega \partial m / \partial p \rangle + \langle \mathrm{LW} \rangle + \langle \mathrm{SW} \rangle + \mathrm{LH} + \mathrm{SH} \tag{5}$$

where the terms on the right-hand side of equation (5) are the vertically integrated horizontal and vertical advection of $\langle m \rangle$, longwave and shortwave radiative heating, and surface turbulent fluxes, respectively.

Moist static energy is approximately conserved during both adiabatic and phase change processes, eliminating the need to accurately measure precipitation. Observational and modeling studies demonstrate that the tropical precipitation rate is a sharply increasing function of column humidity [*Betts*, 1986; *Sherwood*, 1999; *Bretherton et al.*, 2004; *Raymond and Zeng*, 2005; *Holloway and Neelin*, 2009]. The equatorial region has weak Coriolis force and weak temperature gradients, implying that column humidity is primarily responsible for anomalies of $\langle m \rangle$. Results from reduced-complexity models which invoke the “weak temperature gradient” approximation (WTG) [*Sobel et al.*, 2001] support the theory that organized tropical convective disturbances are strongly influenced by the distribution and transport of moisture [*Fuchs and Raymond*, 2005; *Sugiyama*, 2009; *Sobel and Maloney*, 2013]. Subgrid-scale convective processes do not change $\langle m \rangle$ but rather redistribute it within the column. Determining $\partial \langle m \rangle / \partial t$, and by extension key mechanisms that drive large tropical disturbances, can therefore be reduced to an assessment of contributions from $\langle m \rangle$ advection and radiative

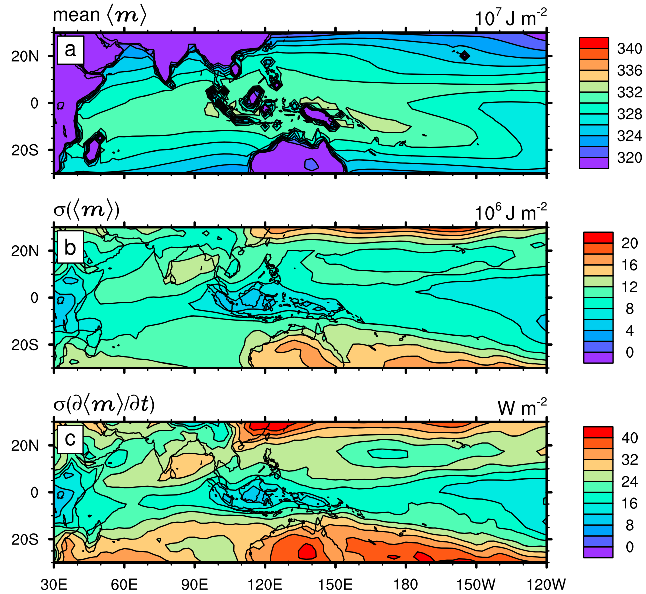

Figure 2. November–April (a) mean $\langle m \rangle$, (b) 20–100 day filtered $\sigma(\langle m \rangle)$, and (c) 20–100 day filtered $\sigma(\partial\langle m \rangle/\partial t)$.

and surface turbulent fluxes [e.g., *Maloney*, 2009; *Kiranmayi and Maloney*, 2011; *Andersen and Kuang*, 2012]. November–April mean $\langle m \rangle$ and standard deviation of $\langle m \rangle$ and $\partial\langle m \rangle/\partial t$ [$\sigma(\langle m \rangle)$, and $\sigma(\partial\langle m \rangle/\partial t)$, respectively] are shown in Figure 2. Maximum $\langle m \rangle$ is collocated with warm SSTs. The $\sigma(\langle m \rangle)$ and $\sigma(\partial\langle m \rangle/\partial t)$ are largest away from the equator, where the WTG assumption begins to break down due to the influence of C_pT associated with extratropical cold air outbreaks. Comparing Figures 2a and 2b indicates that $\langle m \rangle$ varies by about 10% on intraseasonal time scales.

For a propagating disturbance such as the MJO, $\langle m \rangle$ and $\partial\langle m \rangle/\partial t$ are in quadrature. Terms on the right-hand side of equation (5) may vary in phase with $\langle m \rangle$, or in quadrature with $\langle m \rangle$ (i.e., in phase with $\partial\langle m \rangle/\partial t$). Processes that covary most coherently with $\langle m \rangle$ affect the maintenance of MJO convection, while processes that covary most coherently with $\partial\langle m \rangle/\partial t$ are linked to propagation of MJO convection. We use the following conventions for discussing the effects of moisture budget terms on the in-phase and quadrature components of $\langle m \rangle$. When a given process covaries with $\langle m \rangle$ it is said to *maintain*, *sustain*, or *damp* $\langle m \rangle$. A process that covaries with $\partial\langle m \rangle/\partial t$ *generates* or *destroys* $\langle m \rangle$.

3. Results

3.1. Seasonal Means and Intraseasonal Variability at the Air-Sea Interface

Before examining the relationships of surface flux-related variables to the MJO, we present seasonal means and intraseasonal standard deviations of those variables. We analyzed May–October and November–April, but show results only for the latter.

Figures 3a–3e present means and Figures 3f–3j the 20–100 day band-pass filtered standard deviations (σ) of rainfall, near-surface wind speed (we use ERA-I 10 m winds, but using 1000 hPa winds produces similar results), surface latent and sensible heat flux (LH and SH, respectively), and SST. Positive mean zonal 850 hPa wind (u850; contours) is overlaid. Seasonal mean rainfall highlights the familiar intertropical convergence zone (ITCZ) and south Pacific convergence zone (SPCZ), while the standard deviation (hereafter $\sigma(x)$, where x is any 20–100 day filtered variable) of rainfall, σ(rainfall), is distributed more broadly in latitude over these regions. In the Tropics, minimum mean wind speed and, to a lesser degree, $\sigma(|\mathbf{V}|)$ are roughly collocated with maximum u850. This equatorial trough of low mean wind speeds is reflected in a similar equatorial trough of $\overline{\text{LH}}$, especially in the Indian Ocean, whereas the equatorial σ(LH) is zonally uniform throughout the Warm Pool. Maximum 10 m $\overline{|\mathbf{V}|}$ and $\sigma(|\mathbf{V}|)$ at 15°S and 15°N are driven by trade winds and transient disturbances, such as westward propagating equatorial Rossby waves. These subtropical wind features are sometimes linked to winter hemisphere cold air outbreaks and shift the $\overline{\text{LH}}$ and σ(LH) and patterns toward southeast Asia. Because SH is approximately an order of magnitude smaller than LH, SH contour intervals are 10% of those in the LH plots, allowing simple comparisons of their bulk characteristics. $\overline{\text{SH}}$ and σ(SH) do not exhibit as

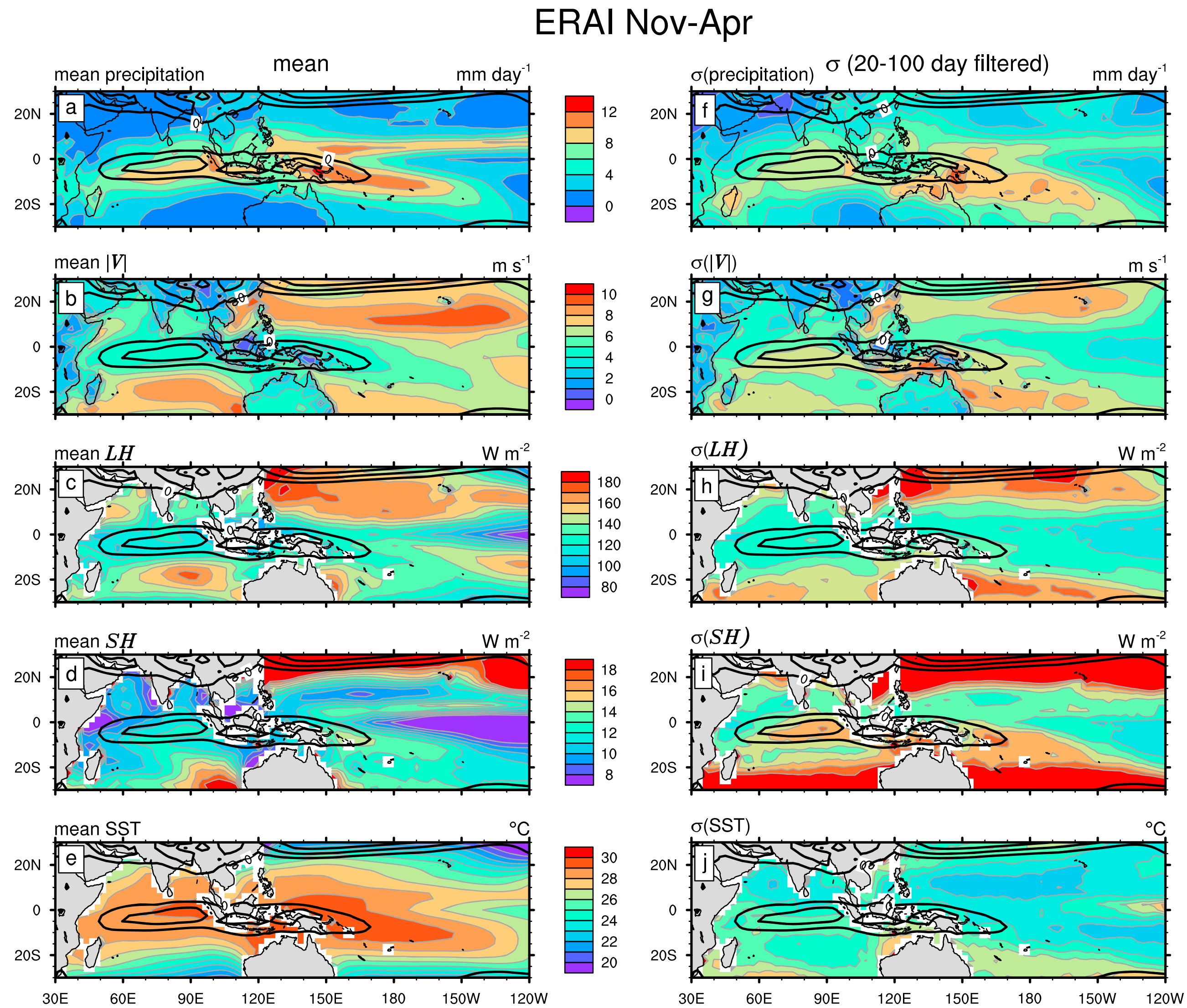

Figure 3. November–April (left column) mean and (right column) 20–100 day standard deviation of (a and f) rainfall, (b and g) 2 m wind speed, (c and h) LH, (d and i) SH, and (e and j) SST. In Figures 3c and 3d, positive fluxes moisten or warm the atmosphere. Mean positive zonal wind at 850 hPa is contoured every 2 m s^{-1} staring at 0 m s^{-1}.

much of an equatorial trough as does LH. This is consistent with the findings of *Young et al.* [1995], *Saxen and Rutledge* [1998], *DeMott et al.* [2014], *Yokoi et al.* [2014], and others, who have noted a greater sensitivity to SST fluctuations for SH than for LH at intraseasonal and shorter time scales. Tropical intraseasonal SST variations are larger in the Indian Ocean than the West Pacific, a consequence of the shallow mixed layer (~30 m) [*de Boyer Montégut et al.*, 2004; *Halkides et al.*, 2015] and possibly the shallower thermocline (~80 m) over the Seychelles-Chagos thermocline ridge (located at ~10°S within the Indian Ocean), and the deeper mixed layer (~40 m) and thermocline (~180 m) in the West Pacific [*McPhaden*, 2002; *Vinayachandran and Saji*, 2008; *Schott et al.*, 2009; *Vialard et al.*, 2012]. Because maximum observed daily mean SST in the Warm Pool is about 30°C [e.g., *Anderson et al.*, 1996; *Sui et al.*, 1997; *de Szoeke et al.*, 2015], the larger σ(SST) in the Indian Ocean arises from more intense intraseasonal cooling events associated with the shallower thermocline [*Duvel et al.*, 2004; *Duvel and Vialard*, 2007; *Drushka et al.*, 2012].

November–April net surface heat flux (Q_{net}) mean and $\sigma(Q_{net})$, and means and standard deviations of its component terms are shown in Figure 4. In the Warm Pool, mean Q_{net} (Figure 4a) is largest in the western Indian Ocean, the Northwest Australia Basin, and just south of the ITCZ in the central and eastern Pacific Ocean. Reduced areas of equatorial Q_{net} largely mimic the patterns of net surface solar and longwave radiation

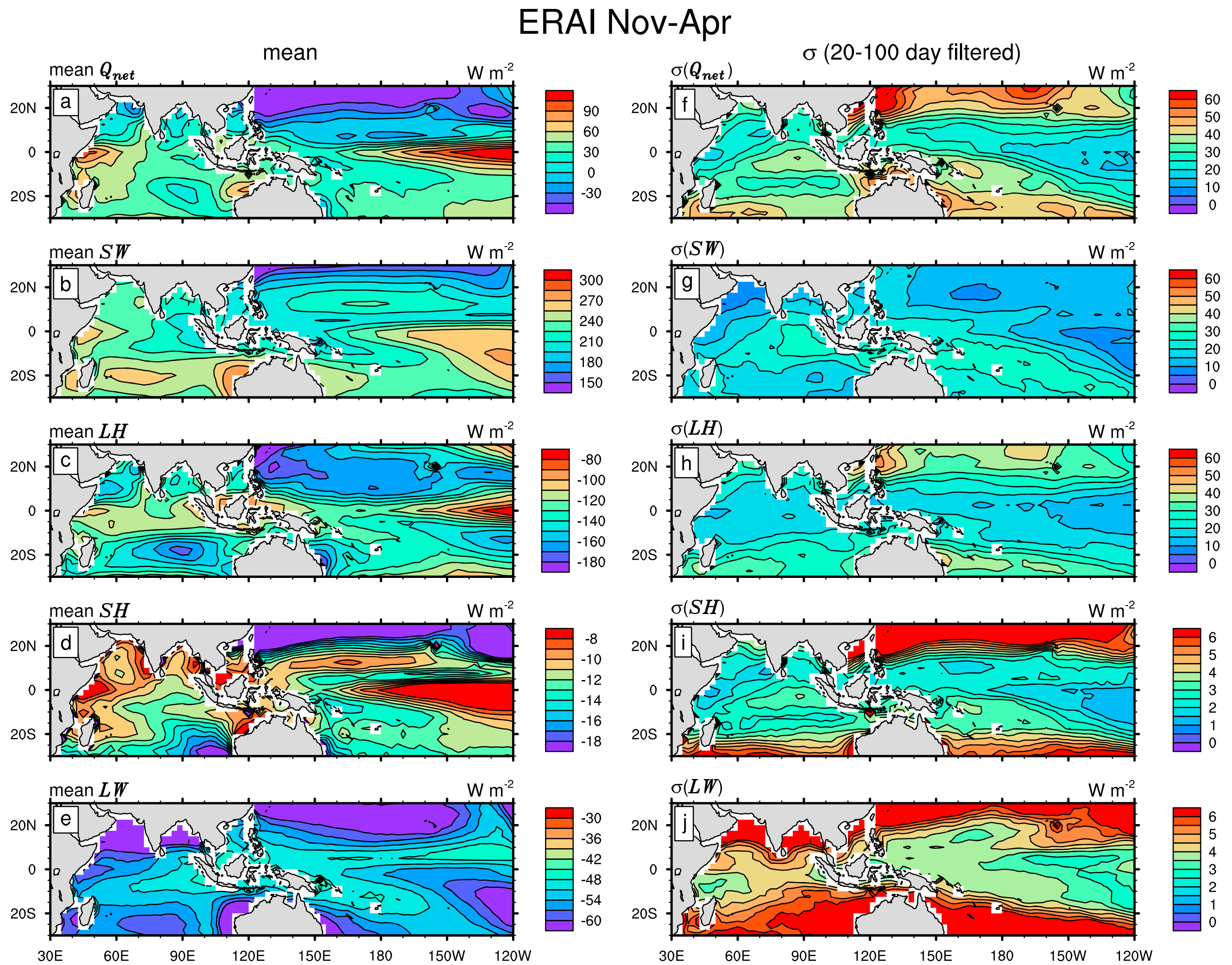

Figure 4. As in Figure 3, but for (a, f) Q_{net}, (b, g) net surface shortwave radiation, (c, h) LH, (d, i) SH, and (e, j) net surface longwave radiation. The 850 hPa zonal winds are omitted. In Figures 4a–4e, positive fluxes warm the ocean.

(Figures 4b and 4e), which are driven by mean cloudiness. Intraseasonal variability of Q_{net}, net surface shortwave radiation, SH, and net surface longwave radiation (Figures 4f, 4g, 4i, and 4j, respectively) maximize along the same Indian Ocean-West Pacific arc as mean longwave surface radiation (Figure 4e), reflecting their tight coupling to MJO cloudiness. In contrast, variability of net surface longwave and latent heat fluxes minimize on the equator. The trough of σ(LH) centered on the equator (Figure 4h) is broader in latitude, reflecting the spatially more extensive $\sigma(|\mathbf{V}|)$.

We next survey the variability of wind-driven, thermodynamic, and second-order flux perturbations for the full and smoothed SST calculations (section 2.2). The degree to which LH can be represented by $\mathrm{LH}^*_{\mathrm{SST}}$ (i.e., the right-hand side of equation (3)) is confirmed by comparing Figures 5a and 5b. The wind-driven flux perturbation ($\overline{\Delta q}|\mathbf{V}|'$; Figure 5c) dominates the thermodynamic ($\Delta q'\overline{|\mathbf{V}|}$; Figure 5d) and second-order ($\Delta q'|\mathbf{V}|'$; Figure 5e) terms. The thermodynamic perturbation ($\Delta q'\overline{|\mathbf{V}|}$) is somewhat larger in the Indian Ocean than in the West Pacific, consistent with the larger Indian Ocean σ(SST) (Figure 3j). The thermodynamic perturbation ($\Delta q'\overline{|\mathbf{V}|}$) is jointly controlled by q_{air} (Figure 5f) and q^*_{SST} (Figure 5g) variations which together drive Δq variability (Figure 5h). Over most of the domain, fluctuations of q_{air} exceed those of q^*_{SST}, as was initially observed with buoy data [*Anderson et al.*, 1996; *Zhang and McPhaden*, 2000]. The q_{air} variability increases with latitude as cold, dry extratropical air is occasionally entrained equatorward by transient disturbances. Only in the South Equatorial Indian Ocean does $\sigma(q^*_{\mathrm{SST}})$ exceed $\sigma(q_{\mathrm{air}})$, suggesting a localized region—approximately the

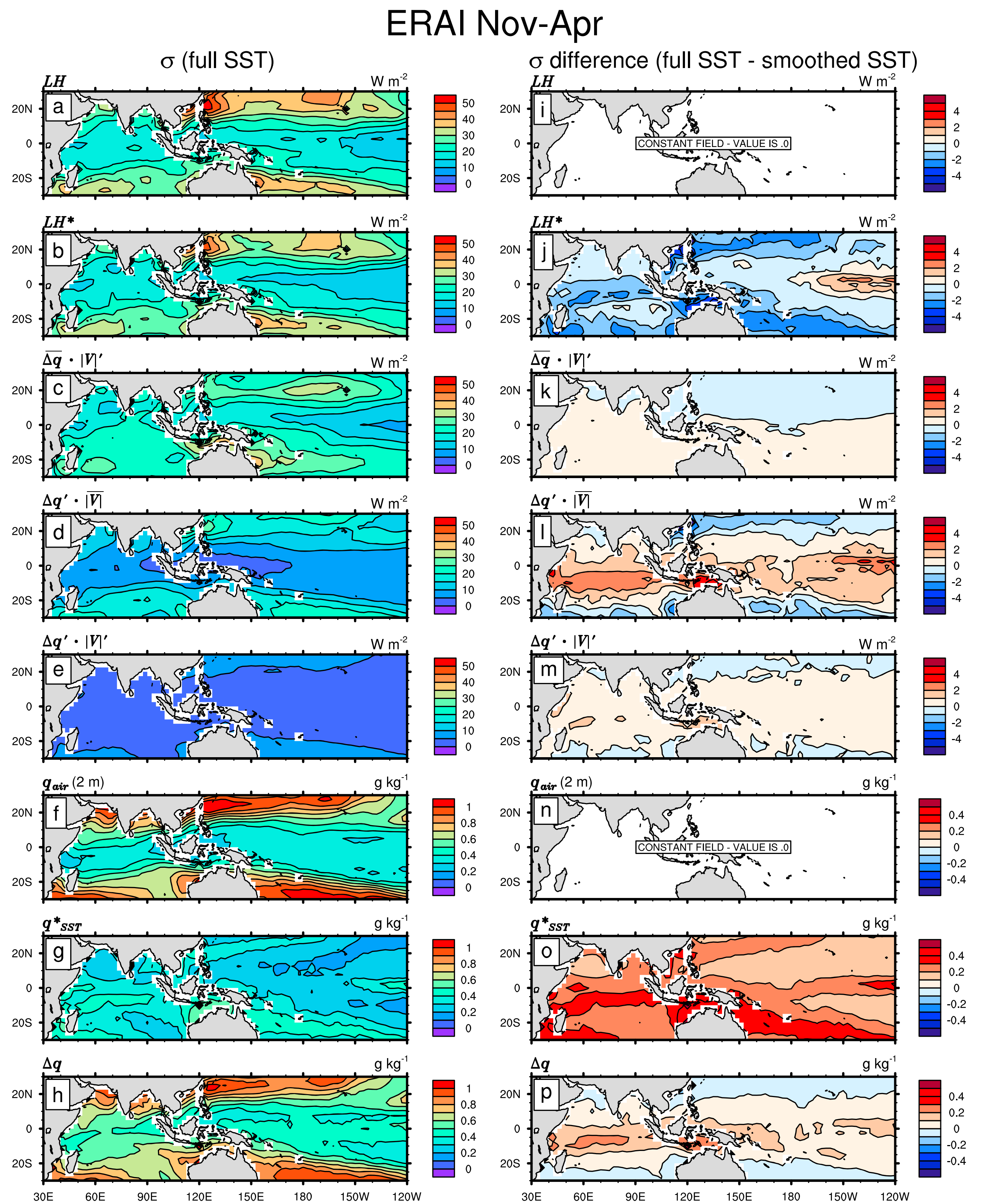

Figure 5. November–April 20–100 day filtered standard deviation of (a) LH; (b) LH*; (c) $\overline{\Delta q}|\mathbf{V}|'$; (d) $\Delta q'\overline{|\mathbf{V}|}$; (e) $\Delta q'|\mathbf{V}|'$; (f) q_{air}; (g) q^*_{SST}; and (h) Δq. In Figures 5b–5h quantities are computed using the "full" SST time series. In Figures 5i–5o the difference between values are plotted in the left column and those computed using 61 day running-mean SST.

Seychelles-Chagos thermocline ridge—of strong ocean control of thermodynamic flux perturbations. The November–April $\sigma(\Delta q)$ (Figure 5h) is not simply the spatial difference of Figures 5f and 5g because the relative phasing of q^*_{SST} and q_{air} varies throughout the Warm Pool [*Hendon and Glick*, 1997]. Phase and amplitude differences between q^*_{SST} and q_{air} combine to produce tropical $\sigma(\Delta q)$ that is largest in the Indian Ocean [*Hendon and Glick*, 1997].

The effect of the smoothed SST time series on component flux terms is shown in Figures 5j–5p as the difference between standard deviations for full and smoothed SST flux terms. The $\sigma(\mathrm{LH}^*_{\mathrm{SST}})$ is 1–2 W m^2 larger than $\sigma(\mathrm{LH}^*_{\overline{\mathrm{SST}}})$ (Figure 5j), yet each of the component terms (Figures 5k–5m) exhibit more equatorial variability with the full SST. The reduction in $\sigma(\mathrm{LH}^*_{\mathrm{SST}})$ is a result of the phase shift of $\Delta q'\overline{|\mathbf{V}|}$ that occurs in the presence of variable SST. The phase shift allows $\Delta q'\overline{|\mathbf{V}|}$ to more effectively offset $\overline{\Delta q}|\mathbf{V}|'$ (Figure 1 and *DeMott et al.*, 2015 [2015, Figure 17]), reducing the total flux amplitude. The SST effect for $\Delta q'\overline{|\mathbf{V}|}$ is most apparent within ∼15° of the equator (Figure 5l). Here variable SSTs enhance $\sigma(\Delta q'\overline{|\mathbf{V}|})$ (the thermodynamic perturbation) by about 2–5 W m^{-2}, which represents a 10%–15% offset of $\sigma(\overline{\Delta q}|\mathbf{V}|')$ (the wind-driven perturbation). A similar analysis is performed for the SH (Figure 6). Variable SSTs contribute about 0.5 W m^{-2} to $\sigma(\Delta T'\overline{|\mathbf{V}|})$ (Figure 6l), which represents up to a ∼20% offset of $\sigma(\overline{\Delta T}|\mathbf{V}|')$.

3.2. Surface Flux and Moist Static Energy Budget Lag Composites

In this section, we review the ocean surface energy balance, the evolution of MSE budget terms, and the impacts of SST variations on surface fluxes over the MJO life cycle. Some elements of this analysis appear elsewhere in the literature (as cited previously), but we present them here to collectively demonstrate the links between surface heating, the ocean response to that heating and its impact on surface fluxes, and the subsequent impact on the MJO MSE budget.

The evolution of the surface energy balance and SST with respect to rainfall in the eastern Indian Ocean is shown in Figure 7. All fluxes are plotted so that positive quantities warm the ocean, and a positive flux into the ocean implies a reduced flux to the atmosphere. During the MJO suppressed phase (lags −20 to −10 days), clear skies and calm winds promote ocean warming via solar radiation and reduced surface turbulent fluxes. Ocean warming by these processes is partially offset by longwave surface cooling. The decrease in LH at −12 days signals the increase of low-level winds and the transition to the MJO active phase. Q_{net} peaks at −15 days and remains positive until −7 days, resulting in a maximum SST anomaly at −7 days. SST cooling begins as soon as Q_{net} becomes negative, but the positive SST anomalies persist until +1 day. Ocean cooling continues until +10 days after rain when Q_{net} again becomes positive. Surface warming by longwave radiation maximizes with peak convection as enhanced clouds and moisture reduce OLR. The phasing and relative amplitude of the intraseasonal net surface energy balance shown in Figure 7 is consistent across most of the Warm Pool, with modest shifts observed in the far western Indian Ocean and over the Maritime Continent (not shown).

The 0.2 K intraseasonal SST range is typical for composites (such as this one) based on values averaged over a broad area of the tropical ocean and covering many events [e.g., *Hendon and Glick*, 1997; *Woolnough et al.*, 2000]. This SST range corresponds to the "foundation SST" representative of a mixed layer, measured mostly by satellites at night, and not the ∼1°C diurnal warm layer observed in the quiescent phase. There is considerable spatial and event-to-event variability [e.g., *de Szoeke et al.*, 2015] of SST fluctuations within the MJO. Geographic variability approximately follows the ocean mixed-layer depth climatology [e.g., *Duvel et al.*, 2004], where shallow mixed layers effectively reduce the upper ocean heat capacity, allowing a larger SST response to a given Q_{net} forcing than would occur with a deep mixed layer and high heat capacity.

It is not uncommon for individual MJO events to exhibit intraseasonal SST ranges of 0.5–1 K at a given point. Intense heating during the MJO suppressed phase can lead to anomalous mixed-layer shoaling [*Anderson et al.*, 1996; *Shinoda and Hendon*, 1998], enabling large positive SST anomalies. A similar effect can arise from strong salinity stratification driven by fresh water fluxes [*Sprintall and Tomczak*, 1992; *Anderson et al.*, 1996; *Zhang and McPhaden*, 2000]. On the other hand, strongly stratified mixed layers can deregulate the SST response to Q_{net} forcing by reducing wind-driven mixing. In these cases, momentum forcing from the atmosphere is trapped in the upper ocean, driving surface currents that can warm or cool the upper ocean by advection [e.g., *McPhaden and Foltz*, 2013; *Moum et al.*, 2013]. These event-to-event idiosyncrasies of the upper ocean state can limit or amplify ocean surface warming during the MJO suppressed phase and likewise enhance or reduce ocean cooling during the active phase [e.g., *Harrison and Vecchi*, 2001; *Saji et al.*, 2006; *Lloyd*

10.1002/2016JD025098

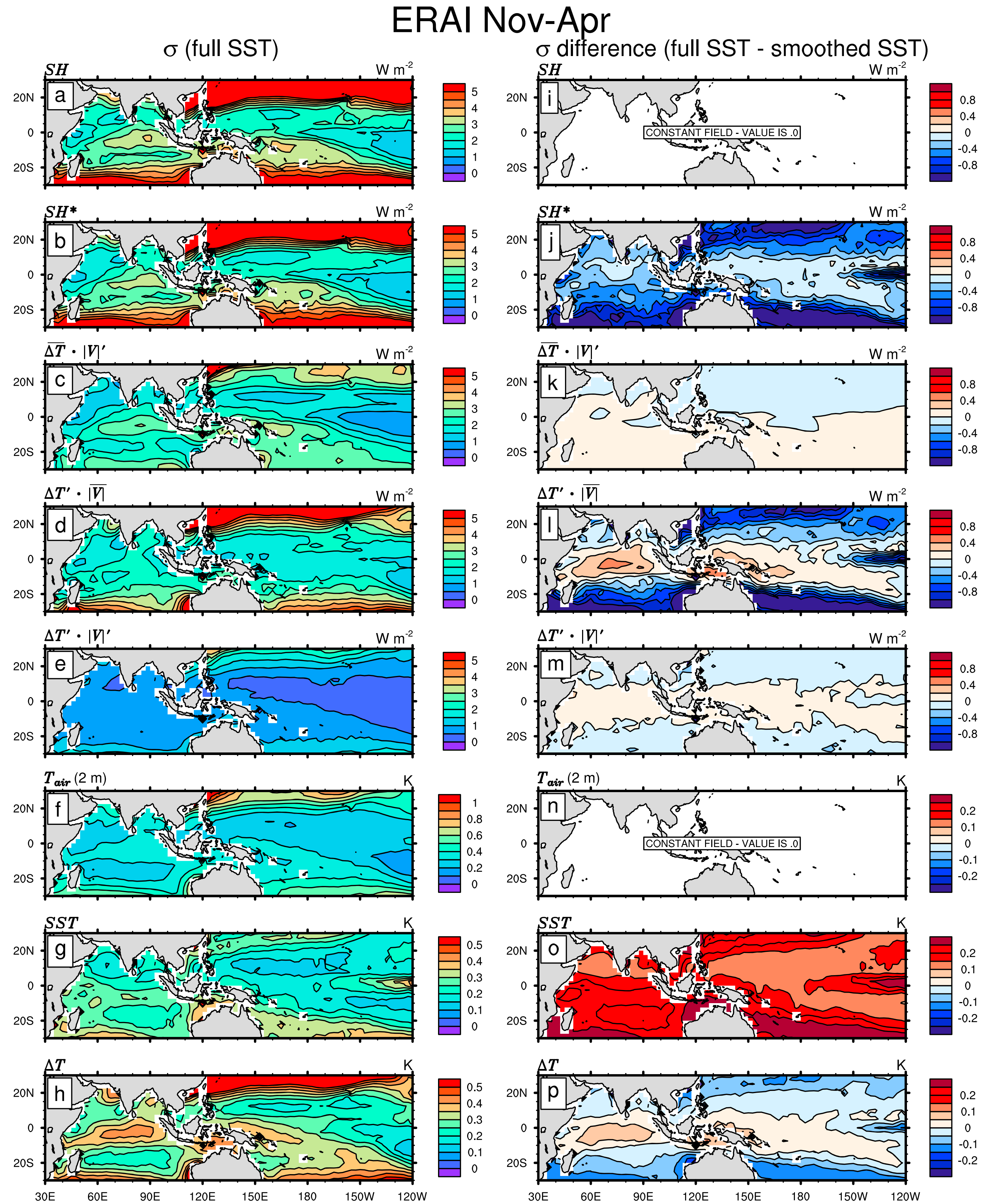

Figure 6. As in Figure 5 but for SH and ΔT.

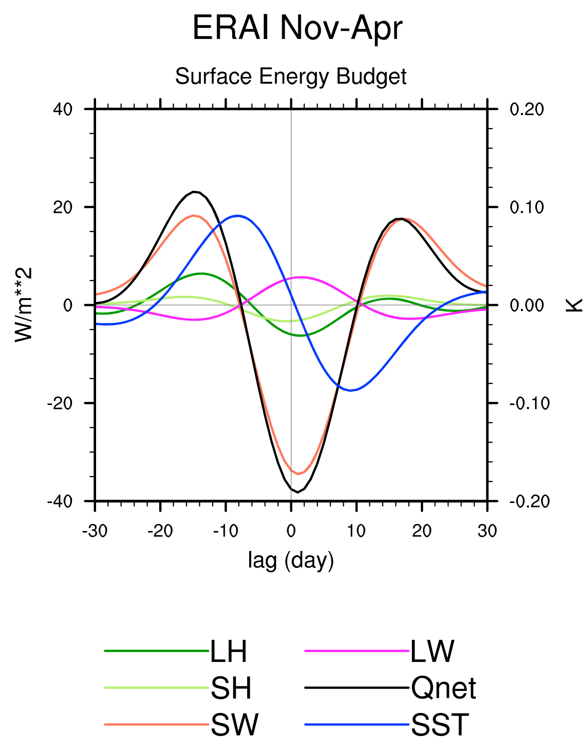

Figure 7. Lagged regression coefficients of surface energy budget terms and SST onto 20–100 day filtered $\langle m \rangle$. Lag = 0 days corresponds to maximum $\langle m \rangle$. Positive flux anomalies warm the ocean.

and Vecchi, 2010; *Koch-Larrouy et al.*, 2011; *McPhaden and Foltz*, 2013; *Seiki et al.*, 2013; *Sprintall et al.*, 2014; *Halkides et al.*, 2015]

Before discussing the effect of SST fluctuations on the MJO, we first review the moist static energy budget of the MJO life cycle. Lag composites of $\langle m \rangle$, $\partial \langle m \rangle / \partial t$, and their budget terms (equation (5)) as a function of longitude are shown in Figure 8. In each panel, shading depicts the regression coefficient of an unfiltered 10°S–10°N averaged variable onto 20–100 day filtered 10°S–10°N averaged rainfall for lags ±30 days, while overlaid contours in all panels are $\langle m \rangle$ regression coefficients. While averaging fields 10°S–10°N obscures potentially important equatorial asymmetries, this widely used presentation format emphasizes the gross temporal evolution of MJO moistening processes as a function of unit heating (i.e., rainfall) and longitude.

The largest $\langle m \rangle$ anomalies per unit heating (contours) are observed in the far western Indian Ocean (Figure 8a), where MJO convection typically initiates [e.g., *Powell and Houze*, 2015]. Approximately 1 week before the onset of western Indian Ocean MJO convection, intense moistening is observed (50°E–70°E; Figure 8f). Here $\partial \langle m \rangle / \partial t$ is almost entirely generated by $-\langle \mathbf{V} \cdot \nabla m \rangle$ (Figures 8c–8e), while the incipient $\langle m \rangle$ anomaly is sustained by column-integrated radiative heating (Figures 8g and 8j). Once MJO convection propagates into the central and eastern Indian Ocean (east of ~60°E), it is chiefly maintained by column radiative heating (especially longwave heating) with secondary contributions from surface fluxes (especially LH, Figure 8h). Generation of $\langle m \rangle$ at negative lags (i.e., $\partial \langle m \rangle / \partial t$ east of convection) is driven primarily by $-\langle \mathbf{V} \cdot \nabla m \rangle$, with secondary contributions from $-\langle \omega \partial m / \partial p \rangle$.

The lag relationship of the wind-driven, thermodynamic, and second-order flux perturbations to $\langle m \rangle$ is shown in Figures 9a–9c. Within the Warm Pool, westerly wind anomalies to the west of MJO heating (i.e., at positive lags) combine with mean state westerlies to produce a positive wind speed anomaly. Consequently, the wind-driven flux perturbation (Figure 9a) maximizes 0–5 days after maximum $\langle m \rangle$, in agreement with similar studies by *Zhang and McPhaden* [2000] and *de Szoeke et al.* [2015]. In contrast, the thermodynamic flux perturbation (Figure 9b) maximizes approximately 10 days prior to maximum $\langle m \rangle$, offsetting the wind-driven perturbation. Second-order flux perturbations (Figure 9c) are an order of magnitude smaller than the wind-driven term, but have phasing similar to the thermodynamic term. The combination of the three flux perturbations is the component total flux (Figure 9d), which generally resembles the wind-driven term.

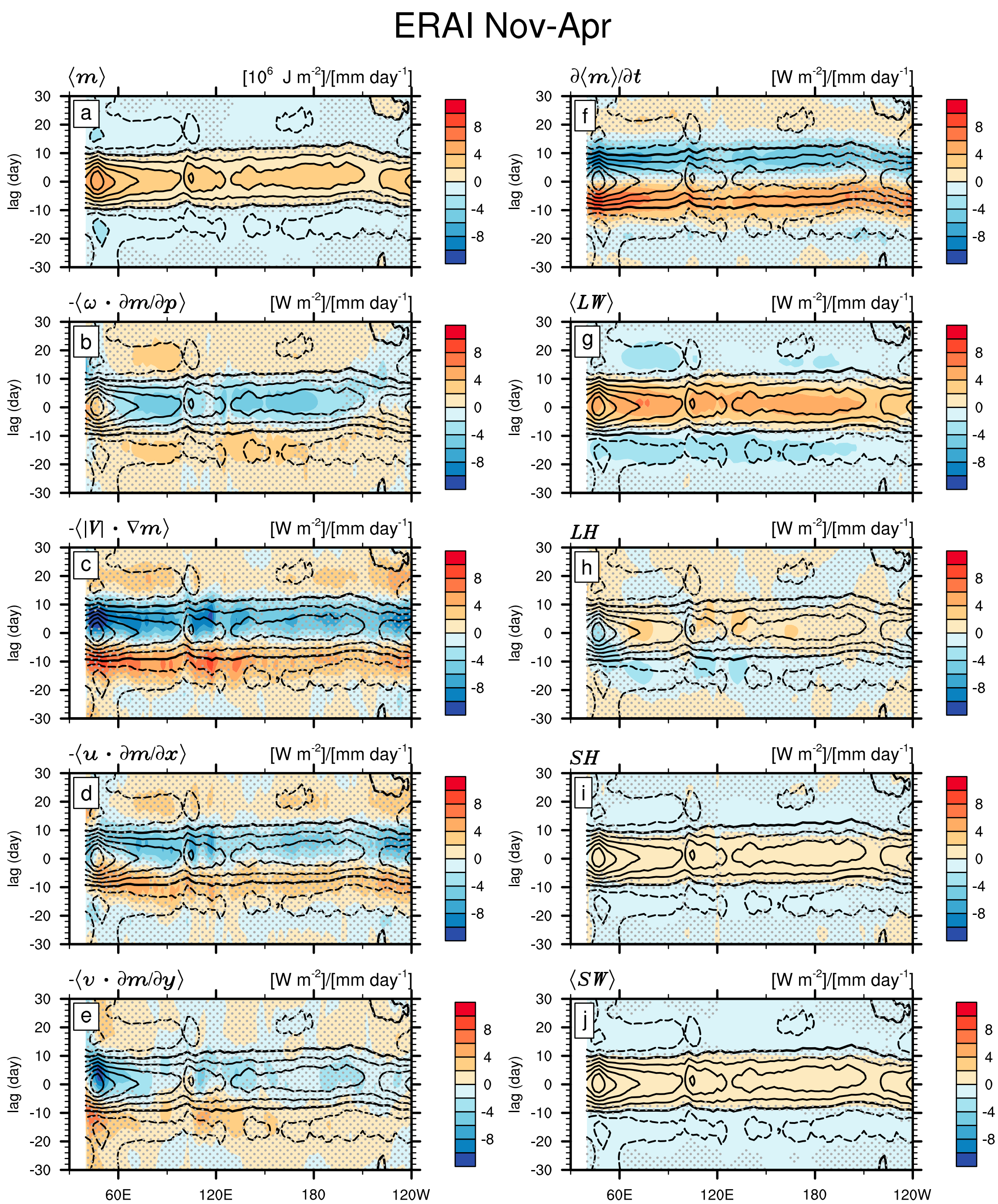

Figure 8. Lagged regression coefficient of vertically integrated 10°S–10°N averaged moist static energy budget terms (equation (5)) onto 20–100 day filtered 10°S–10°N averaged rainfall as a function of longitude: (a) $\langle m \rangle$, (b) $-\langle \omega \partial m/\partial p \rangle$, (c) $-\langle \mathbf{V} \cdot \nabla m \rangle$, (d) $-\langle u \partial m/\partial x \rangle$, (e) $-\langle v \partial m/\partial y \rangle$, (f) $\partial \langle m \rangle/\partial t$, (g) longwave heating (LW), (h) LH, (i) SH, and (j) shortwave heating (SW). Regression coefficient of vertically integrated $\langle m \rangle$ is overlaid (contour interval = 10^6 [J m^2]/[mm day^{-1}]). Stippling masks regions where regression coefficients are not significant at the 95% confidence interval. Zonal rainfall variability is shown in Figure 9g.

$\mathrm{LH}^*_{\overline{\mathrm{SST}}} + \mathrm{SH}^*_{\overline{\mathrm{SST}}}$ (Figure 9e), and its difference from $\mathrm{LH}^*_{\mathrm{SST}} + \mathrm{SH}^*_{\mathrm{SST}}$ (Figure 9f), illustrate the effect of intraseasonal SST variations on MJO surface fluxes. In the far western Indian Ocean (~50°E) during MJO convective initiation, the "SST effect" on surface fluxes and positive $\langle m \rangle$ anomalies maximizes near day 0, suggesting an important role for SST variations during the MJO initiating phase. As convection develops and propagates eastward (50°E–75°E), the SST effect gradually shifts toward more negative lags, where it maintains $\langle m \rangle$ at the leading edge of MJO convection, damps $\langle m \rangle$ at the trailing edge of MJO convection, and generates $\langle m \rangle$ east of convection (Figure 8f).

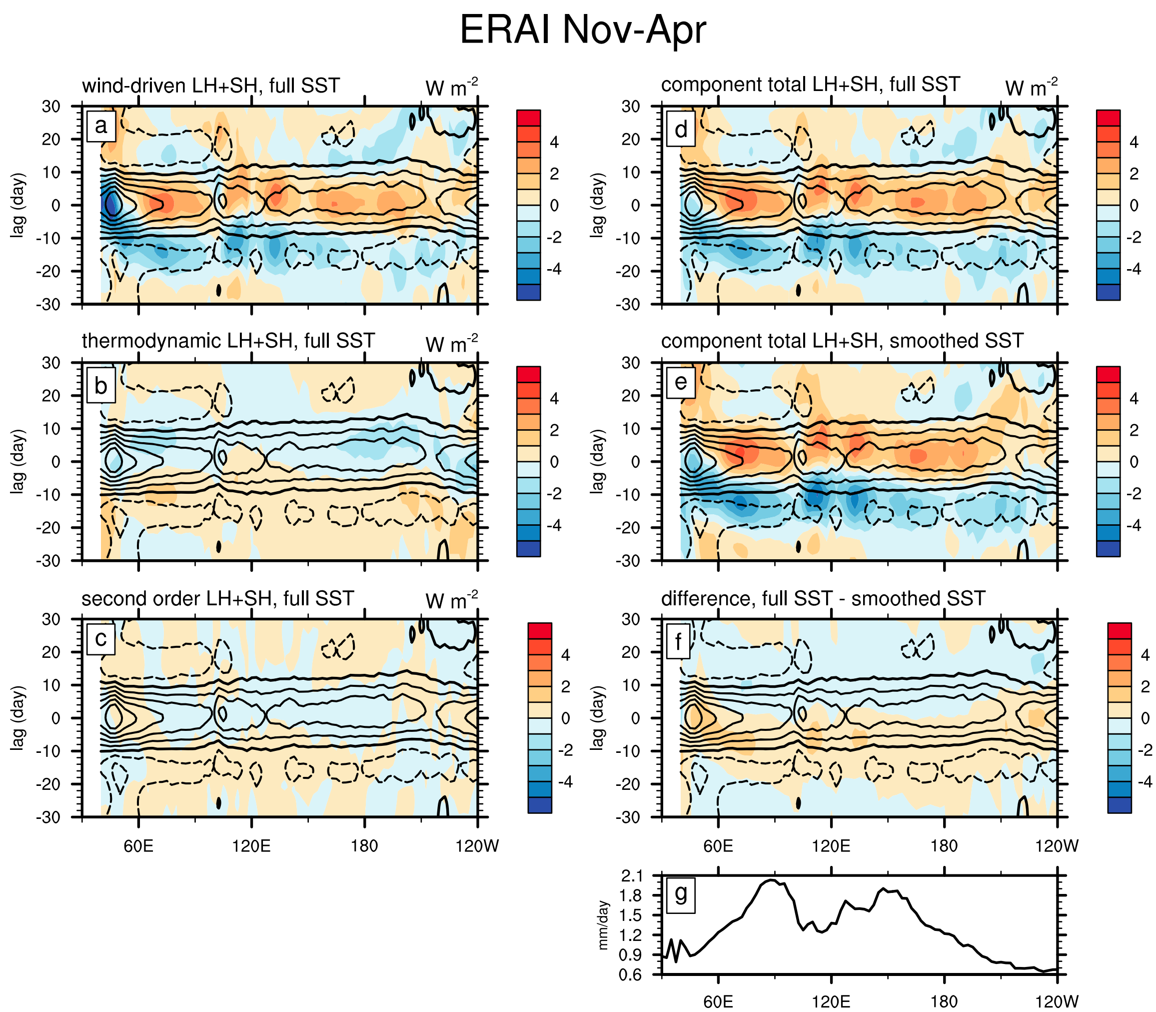

Figure 9. As in Figure 8 but for ocean-only points and (a) $\overline{\Delta q}|\mathbf{V}|' + \overline{\Delta T}|\mathbf{V}|'$ (wind-driven perturbations), (b) $\Delta q'\overline{|\mathbf{V}|} + \Delta T'\overline{|\mathbf{V}|}$ (thermodynamic perturbations), (c) $\Delta q'|\mathbf{V}|' + \Delta T'|\mathbf{V}|'$ (second-order perturbations), (d) the sum of Figures 9a–9c using the full SST calculation ($\mathrm{LH}^*_{\mathrm{SST}} + \mathrm{SH}^*_{\mathrm{SST}}$), (e) the component total flux using the smoothed SST calculation ($\mathrm{LH}^*_{\overline{\mathrm{SST}}} + \mathrm{SH}^*_{\overline{\mathrm{SST}}}$), and (f) the full SST minus smoothed SST difference (Figure 9d − Figure 9e). (g) The 20–100 day filtered 10°S–10°N averaged rainfall standard deviation.

While these results enable a compact assessment of the MJO moist static energy budget and its relation to SST-modulated surface fluxes, interpreting the details of SST impacts is difficult with 10°S–10°N averaged fields. While this is an appropriate latitude band for averaging atmospheric variables, since it roughly encompasses the tropical atmosphere's Rossby radius of deformation, it obscures potentially important oceanic spatial variability, such as that associated with the Seychelles-Chagos thermocline ridge, as well as finer meridional variations associated with the tropical ocean's smaller Rossby radius (∼2°). We are therefore motivated to study the geographic arrangement of SST impacts on $\langle m \rangle$ and $\partial\langle m \rangle/\partial t$.

3.3. Geographic Composites of the Moist Static Energy Budget and SST Effects

In the previous section, the impacts of various moistening processes or SST effects were assessed visually by comparing phasing and amplitude of a given process to $\langle m \rangle$ and $\partial\langle m \rangle/\partial t$. These assessments can be quantified with the regression, R, of a given MSE source term onto $\langle m \rangle$ and $\partial\langle m \rangle/\partial t$, respectively. The fractional maintenance or damping of $\langle m \rangle$ by a given process, P ($F_{\langle m \rangle}(P)$), is obtained by converting $R(\langle m \rangle, P)$ to units of % $\langle m \rangle$ day^{-1}. The fractional amplification or reduction of $\partial\langle m \rangle/\partial t$ ($F_{\partial\langle m \rangle/\partial t}(P)$) is obtained by converting $R(\partial\langle m \rangle/\partial t, P)$ to units of %:

$$F_{\langle m \rangle}(P) = \left[\frac{1}{N}\sum_{i=1}^{N}(P_i \cdot \langle m \rangle_i)/\sigma^2(\langle m \rangle)\right] \cdot 100 \cdot 86,400 \text{ s day}^{-1} \quad (6)$$

$$F_{\partial\langle m\rangle/\partial t}(P) = \left[\frac{1}{N}\sum_{i=1}^{N}(P_i \cdot (\partial\langle m\rangle/\partial t)_i)/\sigma^2(\partial\langle m\rangle/\partial t)\right] \cdot 100 \tag{7}$$

where N is the number of samples in the time series and $\sigma^2(x)$ is the variance of the quantity x.

Andersen and Kuang [2012] first used this method to assess the composite area-integrated $F_{\langle m\rangle}$ and $F_{\partial\langle m\rangle/\partial t}$ of budget terms for aquaplanet MJO simulations, while *Wing and Emanuel* [2014] and *Arnold and Randall* [2015] applied the same method to time-evolving probability distribution functions of budget terms. Here we focus only on the temporal variability of the budget terms at each grid point. Maps of $F_{\langle m\rangle}(P)$ and $F_{\partial\langle m\rangle/\partial t}(P)$ represent the local contributions of a given process to the maintenance (or damping) of $\langle m\rangle$ or to the generation (or destruction) of $\langle m\rangle$ (i.e., contributions to $\partial\langle m\rangle/\partial t$) over the MJO life cycle.

The contributions of budget source terms to 20–100 day filtered $\langle m\rangle$ and $\partial\langle m\rangle/\partial t$ are shown in Figures 10 (left column) and 10 (right column), respectively. The $\langle m\rangle$ is primarily maintained by vertically integrated longwave heating anomalies (Figure 10a) (e.g., *Andersen and Kuang* [2012], *Kim et al.* [2014], *Chikira* [2014], and others). Reduction of column-integrated $\langle m\rangle$ is accomplished by $-\langle\omega\partial m/\partial p\rangle$ over the Warm Pool (Figure 10b) and $-\langle \mathbf{V}\cdot\nabla m\rangle$ across the tropical oceans (Figures 10c–10e). Here and elsewhere in the literature, such processes may be described as "exports" of $\langle m\rangle$; however, for $-\langle\omega\partial m/\partial p\rangle$, this does not indicate transport of $\langle m\rangle$ across the top or bottom column boundaries but rather the integrated effect of vertical motion acting on the $\langle m\rangle$ profile. LH weakly damps $\langle m\rangle$ anomalies across the MJO life cycle, except in the eastern Indian Ocean (Figure 10f), while SH (Figure 10g) and column shortwave heating (Figure 10h) weakly sustain tropical $\langle m\rangle$ anomalies.

Horizontal advection of $\langle m\rangle$, $-\langle \mathbf{V}\cdot\nabla m\rangle$, is the primary regulator of column moistening and drying throughout the MJO life cycle and is dominated by $-\langle u\partial m/\partial x\rangle$ (Figures 10k–10m). This result has been noted in other studies (e.g., *Zhu and Hendon* [2015], who focused on moistening over the Indian Ocean) but is seemingly at odds with *Maloney* [2009], *Kiranmayi and Maloney* [2011], and *Kim et al.* [2014], who document the importance of $-\langle v\partial m/\partial y\rangle$ in the MJO life cycle across the entire Warm Pool. In those studies, a larger $-\langle v\partial m/\partial y\rangle$ than $-\langle u\partial m/\partial x\rangle$ was observed over the West Pacific, but a larger $-\langle u\partial m/\partial x\rangle$ than $-\langle v\partial m/\partial y\rangle$ was observed over the Indian Ocean. None of those studies computed the fractional contributions of those terms to $\partial\langle m\rangle/\partial t$, but visual inspection of lag composite figures in each of those studies reveal more similar phasing of $-\langle u\partial m/\partial x\rangle$ than $-\langle v\partial m/\partial y\rangle$ to $\partial\langle m\rangle/\partial t$ across the MJO life cycle, suggesting larger fractional contributions of $-\langle u\partial m/\partial x\rangle$ to $\partial\langle m\rangle/\partial t$, despite brief periods of strong moistening by $-\langle v\partial m/\partial y\rangle$. It is important to note, therefore, that weak projections over the MJO life cycle do not necessarily imply low importance of a given process across the entire MJO life cycle. We note that this caveat also applies to LH, which is known to peak with maximum MJO rainfall [e.g., *Zhang and McPhaden*, 2000; *DeMott et al.*, 2015] but does not strongly project onto $\langle m\rangle$.

Equatorial $\partial\langle m\rangle/\partial t$ is supported by $-\langle\omega\partial m/\partial p\rangle$ (Figure 10j) driven by the frictional wave-CISK mechanism [*Wang and Rui*, 1990], which is activated by the Kelvin wave response to MJO convection [*Gill*, 1980]. For the eastward moving MJO, $-\langle \mathbf{V}\cdot\nabla m\rangle$ and $-\langle\omega\partial m/\partial p\rangle$ generate $\langle m\rangle$ to the east and destroy $\langle m\rangle$ to the west of MJO convection, which results in MJO propagation across the Warm Pool. Near the equator, however, column longwave heating (Figure 10i) and LH (Figure 10n) destroy $\langle m\rangle$, reducing the tendency to propagate.

Projections of LH* component terms (equation (3)) for the full SST are shown in Figures 11a–11e. Figure 11a is the actual LH, repeated from Figure 10f. The $\mathrm{LH}^*_{\mathrm{SST}}$ projection (Figure 11b) bears a strong resemblance to the LH projection (Figure 11a), confirming that LH is well approximated by $\mathrm{LH}^*_{\mathrm{SST}}$. The region of maximum contribution for $F_{\langle m\rangle}$(LH) (i.e., areas of $\pm 2\%$ d^{-1}) roughly follow the shape of intraseasonal rainfall variability (Figure 3f). Unlike LH and $\mathrm{LH}^*_{\mathrm{SST}}$, $\overline{\Delta q}|\mathbf{V}|'$ (Figure 11c) maintains intraseasonal $\langle m\rangle$ anomalies both on and off of the equator, especially in the Indian and far West Pacific Oceans. In contrast, $\Delta q'\overline{|\mathbf{V}|}$ (Figure 11d) damps $\langle m\rangle$ in those regions, so that the combination of the two leading flux terms produces the weakly positive equatorial contributions for $F_{\langle m\rangle}(\mathrm{LH}^*)$ in the eastern Indian Ocean. Peak contributions for $\overline{\Delta q}|\mathbf{V}|'$ are nearly as large as those for column heating by longwave feedbacks (Figure 10a). Left unchecked, $\overline{\Delta q}|\mathbf{V}|'$ would maintain $\langle m\rangle$ and convection anomalies off the equator, which is an unfavorable heating structure for forcing the equatorial Kelvin wave response that drives MJO propagation. The $\Delta q'\overline{|\mathbf{V}|}$, via its ability to offset large positive $\overline{\Delta q}|\mathbf{V}|'$ anomalies away from the equator, may therefore be a crucial element for damping $\langle m\rangle$ away from the equator and effectively focusing $\langle m\rangle$ onto the equator, which is a favorable heating structure for MJO propagation.

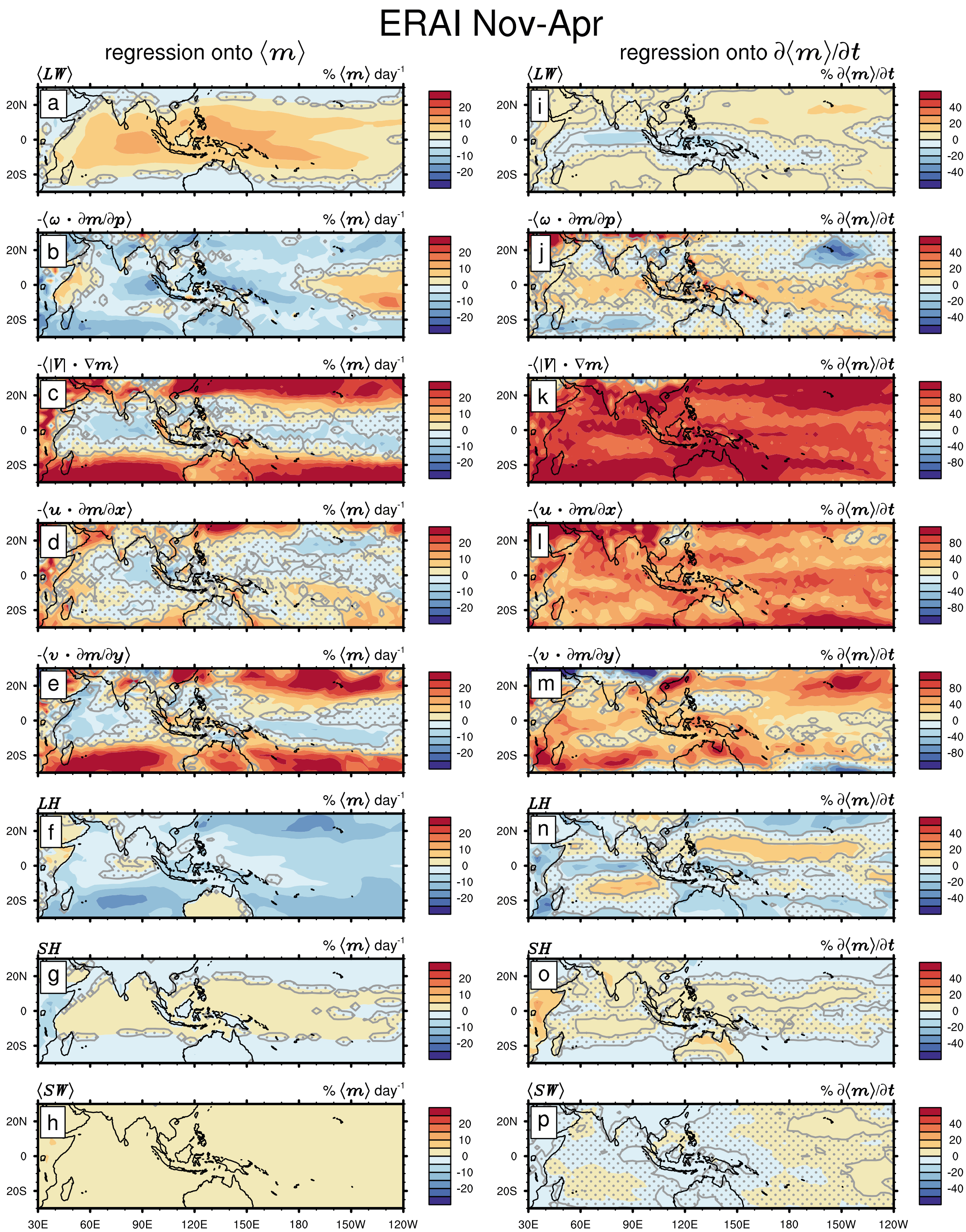

Figure 10. Regression coefficients of $\langle m\rangle$ budget term anomalies regressed onto (left column) 20–100 day filtered $\langle m\rangle$ and (right column) $\partial\langle m\rangle/\partial t$: (a, i) longwave heating; (b, j) $-\langle\omega\partial m/\partial p\rangle$; (c, k) $-\langle\mathbf{V}\cdot\nabla m\rangle$; (d, l) $-\langle u\partial m/\partial x\rangle$; (e, m) $-\langle v\partial m/\partial y\rangle$; (f, n) LH; (g, o) SH; and (h, p) shortwave heating. Note different scale for Figures 10k–10m. Stippling masks areas where regressions are not significant at the 95% confidence interval.

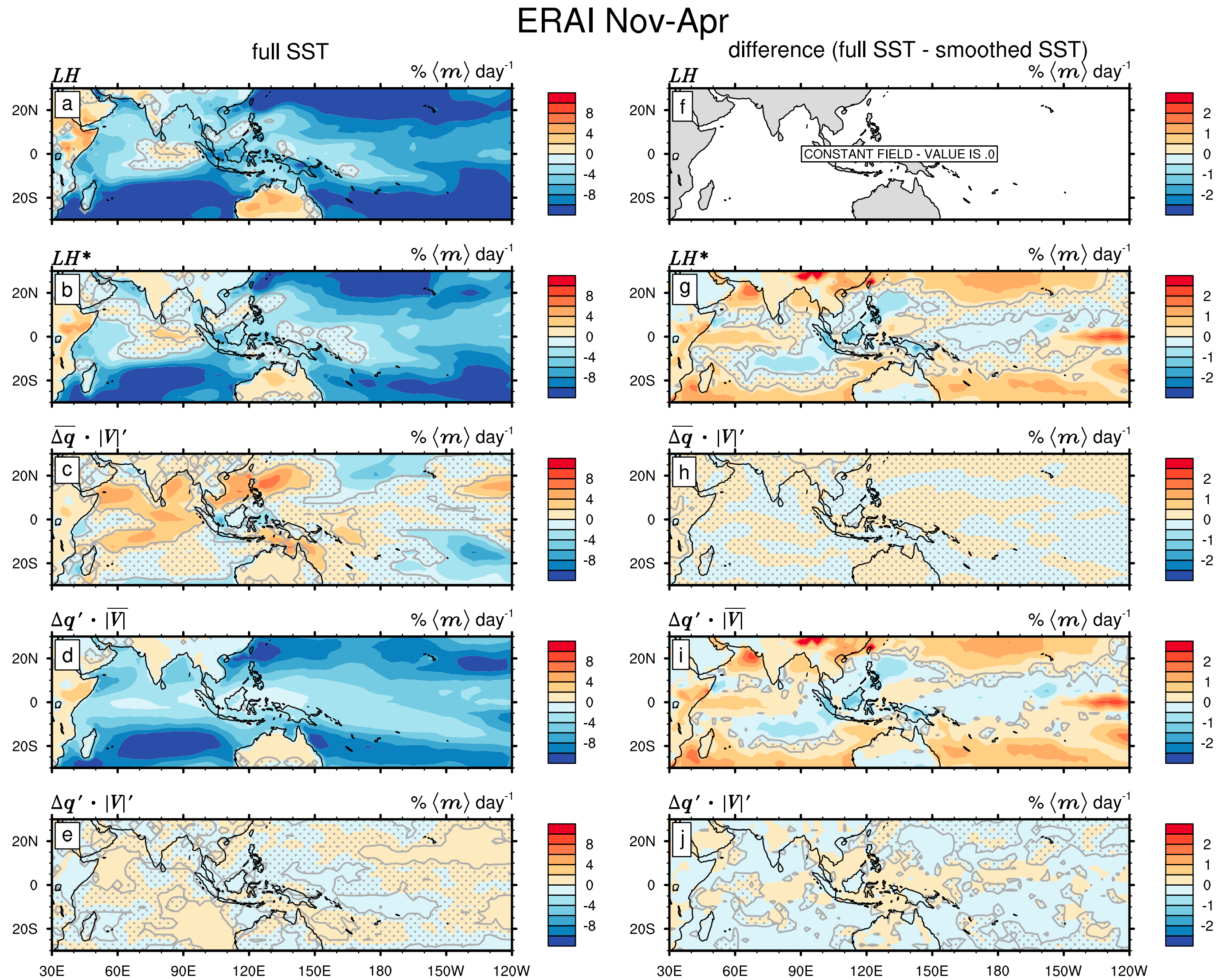

Figure 11. As in Figure 10 but for (a–e) regression coefficients of LH and $\mathrm{LH}^*_{\mathrm{SST}}$ component terms regressed onto 20–100 day filtered $\langle m \rangle$. (f–j) Differences between Figures 11a–11e and component $\mathrm{LH}^*_{\overline{\mathrm{SST}}}$. LH* (Figures 11b and 11g) obtained with Reynolds decomposition (Figures 11c–11e and 11h–11i). Stippling in left (right) column masks regions where regression coefficients (differences of means) are not significant at the 95% confidence interval.

To investigate the role of intraseasonal SST variations within the MJO, we computed the difference between $F_{\langle m \rangle}(\mathrm{LH}^*_{\mathrm{SST}})$ and $F_{\langle m \rangle}(\mathrm{LH}^*_{\overline{\mathrm{SST}}})$ and their component differences (Figures 11f–11j). Positive values of $F_{\langle m \rangle}(\mathrm{LH}^*_{\mathrm{SST}}) - F_{\langle m \rangle}(\mathrm{LH}^*_{\overline{\mathrm{SST}}})$ are observed in the western equatorial Indian Ocean, in and around the Maritime Continent, and in the far West Pacific (Figure 11g). In the western Indian Ocean, SST perturbations help maintain $\langle m \rangle$ anomalies on the equator, and damp them off of the equator. Damping of $\langle m \rangle$ by SST (negative values of $F_{\langle m \rangle}(\mathrm{LH}^*_{\mathrm{SST}}) - F_{\langle m \rangle}(\mathrm{LH}^*_{\overline{\mathrm{SST}}})$) occurs within atmospheric equatorial Rossby and mixed-Rossby gravity wave tracks [*Wheeler and Hendon*, 2004], suggesting that wind-driven ocean cooling within these disturbances initiates a negative feedback response to convective heating, consistent with the findings of *Batstone et al.* [2005]. The $\pm 2\%$ of daily $\langle m \rangle$ attributable to SST fluctuations represents 10%–25% of LH* contributions to the $\langle m \rangle$ budget.

The total effect of SST-modulated surface fluxes is shown in Figure 12 as the differences in $F_{\langle m \rangle}(\mathrm{LH}^*)$ and $F_{\langle m \rangle}(\mathrm{SH}^*)$ contributions for full SST and smoothed SST flux estimates. SST contributions to $F_{\langle m \rangle}(\mathrm{SH}^*)$ and $F_{\partial \langle m \rangle / \partial t}(\mathrm{SH}^*)$ (Figures 12b and 12e, respectively) are approximately 25% of those for $F_{\langle m \rangle}(\mathrm{LH}^*)$ and $F_{\partial \langle m \rangle / \partial t}(\mathrm{LH}^*)$, with similar spatial patterns, so that they reinforce the SST effect on LH* (Figures 12c and 12f). SST contributions to $F_{\partial \langle m \rangle / \partial t}(\mathrm{LH}^* + \mathrm{SH}^*)$ are largest over the eastern Indian Ocean, northwest tropical Pacific, and the northwest Australia basin, where SST variability accounts for $\approx$10% of $\partial \langle m \rangle / \partial t$. SST variations also

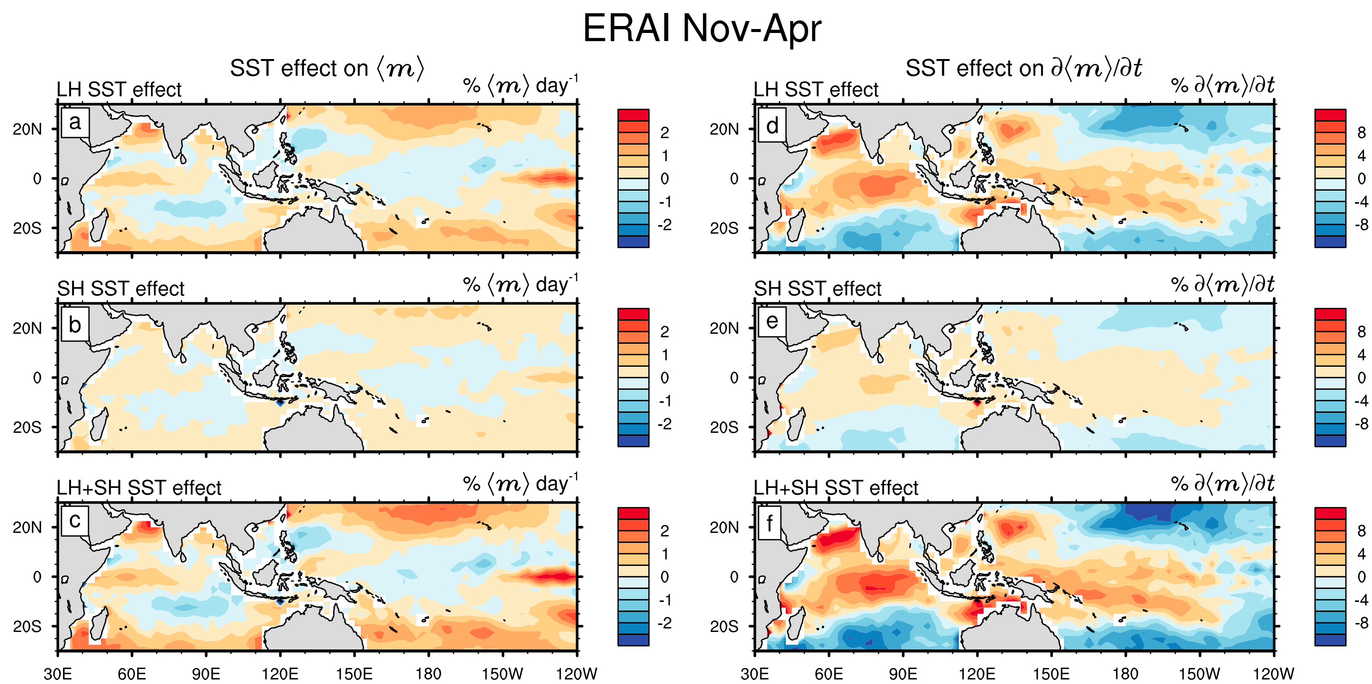

Figure 12. The SST effect on $\langle m \rangle$ (left column) and $\partial\langle m \rangle/\partial t$ (right column) for (a, d) LH*, (b, e) SH*, and (c, f) their sum. As in Figure 11l, the SST effect is calculated as the difference between $F_m(\mathrm{LH}^*_{\mathrm{SST}} + \mathrm{SH}^*_{\mathrm{SST}})$ and $F_m(\mathrm{LH}^*_{\underline{\mathrm{SST}}} + \mathrm{SH}^*_{\underline{\mathrm{SST}}})$, and $F_{\partial m/\partial t}(\mathrm{LH}^*_{\mathrm{SST}} + \mathrm{SH}^*_{\mathrm{SST}})$ and $F_{\partial m/\partial t}(\mathrm{LH}^*_{\underline{\mathrm{SST}}} + \mathrm{SH}^*_{\underline{\mathrm{SST}}})$, respectively.

project strongly onto $\langle m \rangle$ and $\partial\langle m \rangle/\partial t$ in the northern Arabian Sea. The large contributions in this regions could reflect the influence of late autumn and early spring boreal summer MJO events, which propagate northward as well as eastward. Alternatively, they could be associated with other phenomena not directly linked to the MJO.

4. Discussion

4.1. Interpreting the SST Effect

The analysis presented in section 3 examines the impact of variable SST on $\langle m \rangle$ and $\partial\langle m \rangle/\partial t$ within the MJO. The former is important for understanding the processes that maintain the $\langle m \rangle$ anomaly throughout the MJO life cycle, while the latter is related to processes that precondition the environment for convection and enable MJO eastward propagation. One can ascertain whether a given process is more important for MJO maintenance or propagation by comparing the magnitude of $F_{\langle m \rangle}(P)$ and $F_{\partial\langle m \rangle/\partial t}(P)$. Before doing so, however, it is helpful to consider what fraction of $\langle m \rangle$ must be maintained per day to sustain the convective anomaly. In their analysis of Indian Ocean MJO surface flux feedbacks, *Riley Dellaripa and Maloney* [2015] argue that one approach to understanding the role of LH is to compare column moistening by LH to column drying by $-\langle \omega \partial m/\partial p \rangle$. Figure 10b indicates $-\langle \omega \partial m/\partial p \rangle$ exports roughly 10% of $\langle m \rangle$ per day throughout the Warm Pool, and up to 20% d^{-1} in the eastern Indian Ocean. Therefore, the modest column moistening by LH in the eastern Indian Ocean (≈5% d^{-1}) offsets a substantial 25% of $\langle m \rangle$ depletion by $-\langle \omega \partial m/\partial p \rangle$. If SST contributions to $\langle m \rangle$ maintenance (Figures 12a-12c) are scaled by the mean Warm Pool $-\langle \omega \partial m/\partial p \rangle$ (i.e., divided by 0.1–0.2), the SST effects to $F_{\langle m \rangle}$ and $F_{\partial\langle m \rangle/\partial t}$ are more directly comparable and suggest similar fractional contributions to $\langle m \rangle$ maintenance by SST compared to $\partial\langle m \rangle/\partial t$.

An alternative method for measuring the relative importance of SST fluctuations to $\langle m \rangle$ or $\partial\langle m \rangle/\partial t$ is achieved through modifications to the quantity in the square brackets in equations (6) and (7). In those equations, dividing the summation of products $P \cdot \langle m \rangle$ and $P \cdot \partial\langle m \rangle/\partial t$ by variances $\sigma^2(\langle m \rangle)$ and $\sigma^2(\partial\langle m \rangle/\partial t)$, respectively, yields units of % $\langle m \rangle$ d^{-1} and % $\partial\langle m \rangle/\partial t$, which cannot be compared directly. If we instead divide each product by its respective standard deviation, $\sigma(\langle m \rangle)$ or $\sigma(\partial\langle m \rangle/\partial t)$, both results have units of P. We refer to these new quantities as normalized projections, denoted by $\tilde{F}_{\langle m \rangle}(P)$ and $\tilde{F}_{\partial\langle m \rangle/\partial t}(P)$. The SST effect on $\langle m \rangle$ and $\partial\langle m \rangle/\partial t$ using this alternative method is shown in Figure 13. The SST effect for both $\tilde{F}_{\langle m \rangle}$ and $\tilde{F}_{\partial\langle m \rangle/\partial t}$ is O(1 W m^2) throughout the Warm Pool, indicating roughly similar contributions of SST perturbations

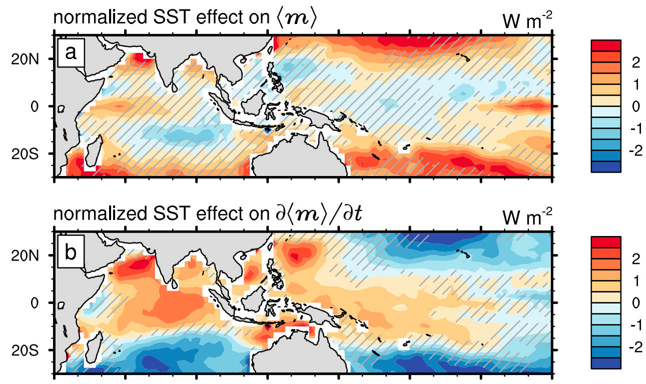

Figure 13. Normalized projections of the SST effect, defined as the differences between $\tilde{F}_m(\mathrm{LH}^*_{\mathrm{SST}} + \mathrm{SH}^*_{\mathrm{SST}})$ and $\tilde{F}_m(\mathrm{LH}^*_{\underline{\mathrm{SST}}} + \mathrm{SH}^*_{\underline{\mathrm{SST}}})$, and $\tilde{F}_{\partial m/\partial t}(\mathrm{LH}^*_{\mathrm{SST}} + \mathrm{SH}^*_{\mathrm{SST}})$ and $\tilde{F}_{\partial m/\partial t}(\mathrm{LH}^*_{\underline{\mathrm{SST}}} + \mathrm{SH}^*_{\underline{\mathrm{SST}}})$, respectively. (a) Hatching masks regions where the projection is larger for $\partial\langle m \rangle/\partial t$. (b) Hatching masks regions where the projection is larger for $\langle m \rangle$.

to $\langle m \rangle$ and $\partial\langle m \rangle/\partial t$. $\tilde{F}_{\langle m \rangle}$ is shown in Figure 13a and hatching masks areas where the SST effect is larger for $\partial\langle m \rangle/\partial t$ (i.e., $|\tilde{F}_{\partial\langle m \rangle/\partial t}| > |\tilde{F}_{\langle m \rangle}|$). Unhatched areas in Figure 13a indicate that SST-modified surface fluxes have a larger impact on $\langle m \rangle$ in the western equatorial Indian Ocean and southern West Pacific (5°S–15°S, 160°E), where they maintain $\langle m \rangle$ and over the Seychelles-Chagos thermocline ridge and northern West Pacific (15°N, 160°E), where they damp $\langle m \rangle$. Over most of the Warm Pool, the SST effect has a larger impact on $\partial\langle m \rangle/\partial t$ and MJO propagation, especially in the Indian Ocean (Figure 13b; areas where $|\tilde{F}_{\langle m \rangle}| > |\tilde{F}_{\partial\langle m \rangle/\partial t}|$ are hatched).

These results suggest that SST anomalies have a *direct* effect on the development of MJO convection in the western Indian Ocean, the focusing of MJO convection onto the equator, and the maintenance and propagation of convection beyond the Maritime Continent. The preferential maintenance of $\langle m \rangle$ on the equator in the Indian Ocean promotes a favorable heating arrangement for forcing the east-of-convection Kelvin wave that drives low-level convergence, shallow convection, and the gradual moistening of the free troposphere via the frictional wave-CISK mechanism [*Wang and Xie*, 1998; *Marshall et al.*, 2008; *Lappen and Schumacher*, 2012, 2014]. This "equatorial focusing" effect of ocean coupling was observed by *Benedict and Randall* [2011] when they coupled their atmosphere-only version of the superparameterized Community Atmosphere Model to a slab ocean model. In that study, MJO convection along the equator was enhanced and eastward MJO propagation was more coherent in the coupled simulation than in the atmosphere-only simulation (i.e., their Figure 10). East of MJO convection, SST perturbations also enhance $\partial\langle m \rangle/\partial t$ by offsetting negative $\overline{\Delta q}|\mathbf{V}|'$ anomalies (e.g., Figure 9) and increasing the efficiency of column moistening during the MJO suppressed phase.

SST perturbations may also have *indirect* impacts on the MJO, either by amplifying the more dominant atmospheric processes that maintain and propagate MJO convection or via other processes that rectify onto the MJO. Examples of the former include the generation of larger stratiform cloud decks and their longwave heating feedbacks [*Del Genio and Chen*, 2015; *Kim et al.*, 2015; *Crueger and Stevens*, 2015] and enhancement of midlevel moistening by $-\langle \mathbf{V} \cdot \nabla m \rangle$ [e.g., *DeMott et al.*, 2014; *de Szoeke et al.*, 2015; *Zhu and Hendon*, 2015]. SST-driven processes that could rectify onto the MJO include the effects of diurnal warm layers [*Sui et al.*, 1997; *Bellenger and Duvel*, 2009; *Bellenger et al.*, 2010; *Ruppert and Johnson*, 2015], which moisten the lower atmosphere by forcing a diurnal cycle of convection and SST gradient-driven moisture convergence [*Lindzen and Nigam*, 1987; *Back and Bretherton*, 2009; *Hsu and Li*, 2012; *Li and Carbone*, 2012].

4.2. Potential Impacts of Uncertainties in Reanalysis Fluxes

Comparisons of monthly LH and SH to buoy measurements indicate that ocean-to-atmosphere fluxes in ERA-Interim may be too large [*Brunke et al.*, 2011; *Chaudhuri et al.*, 2013; *Kent et al.*, 2013; *Brown and Kummerow*, 2014; *Valdivieso et al.*, 2015]. LH and SH biases are primarily driven by a dry bias in q_{air} and a warm bias in T_{air}, respectively. These biases are partially mitigated by a negative wind speed bias in the reanalysis. This has several ramifications for our findings. First, surface flux contributions to intraseasonal $\langle m \rangle$ and $\partial\langle m \rangle/\partial t$ may be overestimated, although regressing surface fluxes onto intraseasonal rainfall (not shown) yields coefficients very similar to those reported in *Riley Dellaripa and Maloney* [2015] based on buoy measurements. Second, the mean state biases in q_{air} and T_{air} imply an overestimate of $\overline{\Delta q}$ and $\overline{\Delta T}$, and therefore an overestimate of

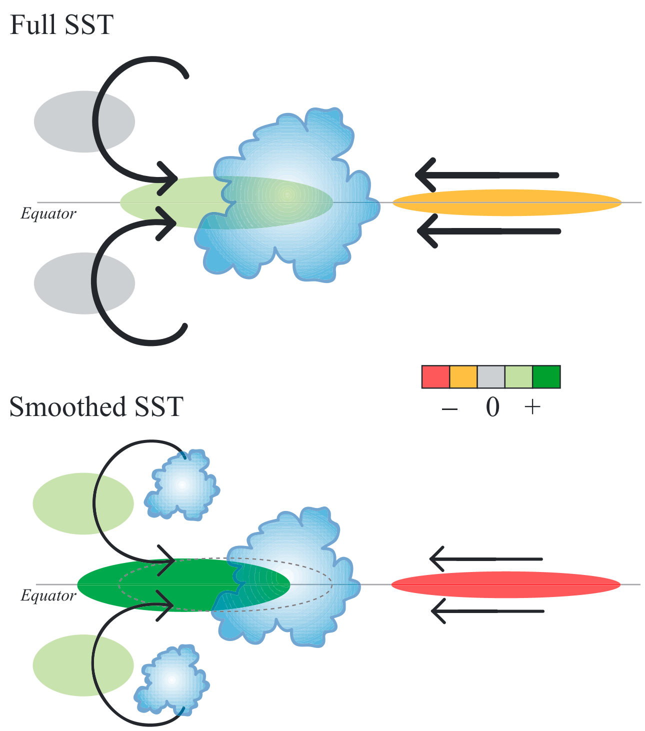

Figure 14. Schematic illustration of the effects of variable SSTs on surface fluxes within the MJO. Cloud elements represent the location and qualitative magnitude of MJO cloudiness and moist static energy anomalies. Arrows depict anomalous low-level circulations forced by MJO heating (weight of arrow is proportional to strength of circulation). Shaded ovals denote regions of anomalous surface fluxes; green (orange/red) shading indicates anomalously positive (negative) fluxes to the atmosphere. (top) Cloudiness, wind, and surface flux anomalies for variable (full) SST. (bottom) Cloudiness, wind, and surface flux anomalies for smoothed SSTs. Dashed oval traces the region of enhanced equatorial surface fluxes in the full SST case.

the wind-driven flux perturbation (e.g., $\overline{\Delta q}|\mathbf{V}|'$). Conversely, the negative bias in mean wind speed implies an underestimate of the thermodynamic flux perturbations ($\Delta q'\overline{|\mathbf{V}|}$). These considerations lead us to believe that contributions of the thermodynamic flux perturbation, and therefore the "SST effect" (Figure 12), may be slightly underestimated.

5. Summary

The role of intraseasonal SST fluctuations within the MJO is studied with ERA-I reanalysis data in the context of the moist static energy budget for the boreal winter (November–April) season. Maps of seasonal means and standard deviations of variables linked to surface flux processes reveal considerable spatial inhomogeneity throughout the Warm Pool, reflecting the influences of land masses, climatological circulations, and ocean stratification.

Surface flux thermodynamic effects, including those rooted in SST variability, are separated from wind effects with the aid of Reynolds decomposition of surface fluxes. SST fluctuations affect wind-driven ($\overline{\Delta q}|\mathbf{V}|'$), thermodynamic ($\Delta q'\overline{|\mathbf{V}|}$), and second-order ($\Delta q'|\mathbf{V}|'$) latent heat flux perturbations through their effect on Δq, and sensible heat flux components through their effect on ΔT. For both latent and sensible heat fluxes, the thermodynamic perturbation is smaller than the wind-driven perturbation, but its different phasing results in a reduction of the wind-driven perturbation and a nonnegligible phase shift of the total flux so that it peaks closer (in both space and time) to MJO convection. Recomputing the component flux terms with a 61 day running-mean filter applied to SST produces a weaker, phase-shifted thermodynamic perturbation. The smaller amplitude and the phase shift of the SST-smoothed thermodynamic perturbation reduces its ability to offset the wind-driven perturbation. The offset of the wind-driven term by the thermodynamic term is strongest around $\pm15°$ latitude, preferentially maintaining moist static energy and convection on the equator.

SST contributions to MJO maintenance and propagation are estimated by projecting full and smoothed SST flux time series onto the intraseasonal $\langle m \rangle$ and $\partial\langle m \rangle/\partial t$ and plotting their differences. These differences represent the SST effect, which is almost entirely encapsulated in the thermodynamic flux perturbation (i.e., $\Delta q'\overline{|\mathbf{V}|}$ and $\Delta T'\overline{|\mathbf{V}|}$). The SST effect maintains 1–2% of daily $\langle m \rangle$ on the equator but damps 1–2% of daily $\langle m \rangle$ off of the equator. Atmospheric vertical advection exports approximately 10% of $\langle m \rangle$ per day, implying that SST fluctuations can offset up to 10–20% of $\langle m \rangle$ depletion by $-\langle \omega \partial m/\partial p \rangle$ on the equator and contribute an additional 10–20% of $\langle m \rangle$ depletion compared to $-\langle \omega \partial m/\partial p \rangle$ off of the equator. The SST effect accounts for 5–10% of intraseasonal $\partial\langle m \rangle/\partial t$, which promotes MJO propagation. These modest contributions of variable SSTs to MJO maintenance and propagation support the paradigm that the MJO is driven primarily by atmospheric processes but is nonnegligibly impacted by ocean feedbacks.

The effects of variable versus fixed SSTs on MJO surface fluxes are contrasted schematically in Figure 14. On the equator, SST perturbations induce an eastward shift of positive surface fluxes so that they are more aligned with convection. This effect is consistent with a positive feedback of SST to MJO convection via the modified WISHE process, in which surface fluxes directly maintain $\langle m \rangle$ and MJO convection. Away from the equator, a negative SST feedback damps $\langle m \rangle$ and weakens off-equator convection. This equatorial "focusing effect" of the SST can reinforce the circulation anomalies that moisten the preconvective environment and promote MJO propagation. East of convection, warm SST anomalies further contribute to column moistening and MJO propagation by increasing suppressed phase surface fluxes.

This study focused on the direct effects of SST perturbations on surface fluxes within the MJO. Other SST-related processes may be at work, such as boundary layer convergence or divergence forced by SST gradients and the emergence of a large SST diurnal cycle during the MJO suppressed phase. Ongoing efforts are focused on closer inspection of these processes and on their frequency of occurrence from one MJO event to the next. The methods developed here can diagnose the role of ocean coupling in model simulations of the MJO and help assess atmospheric and oceanic contributions to simulated MJO characteristics.

Acknowledgments
C.A.D. was supported by NSF award AGS-1445191. J.J.B. was supported by NSF award AGS-1547910. N.P.K. was supported by an Independent Research Fellowship from the UK Natural Environment Research Council (NE/L010976/1). D.A.R. was supported by National Science Foundation Science and Technology Center for Multi-Scale Modeling of Atmospheric Processes, managed by Colorado State University under cooperative agreement ATM-0425247. S.J.W. was supported by the National Centre for Atmospheric Science, a Natural Environment Research Council collaborative centre, under contract R8/H12/83/001. ERA-Interim data were provided courtesy of ECMWF and can be accessed at http://www.ecmwf.int/en/research/climate-reanalysis/era-interim. We thank Emily Riley Dellaripa, Eric Maloney, Walter Hannah, and Tim Li for insightful discussions regarding this work. Comments from three reviewers improved our understanding and presentation of these results.

References

Andersen, J. A., and Z. Kuang (2012), Moist static energy budget of MJO-like disturbances in the atmosphere of a zonally symmetric aquaplanet, *J. Clim.*, *25*, 2782–2804.
Anderson, S. P., R. A. Weller, and R. B. Lukas (1996), Surface buoyancy forcing and the mixed layer of the western Pacific Warm Pool: Observations and 1D model results, *J. Clim.*, *9*, 3056–3085.
Araligidad, N. M., and E. D. Maloney (2008), Wind-driven latent heat flux and the intraseasonal oscillation, *Geophys. Res. Lett.*, *35*, L04815, doi:10.1029/2007GL032746.
Arnold, N. P., and D. A. Randall (2015), Global-scale convective aggregation: Implications for the Madden-Julian oscillation, *J. Adv. Model. Earth Syst.*, *7*, 1499–1518, doi:10.1002/2015MS000498.
Back, L. E., and C. S. Bretherton (2009), On the relationship between SST gradients, boundary layer winds, and convergence over the tropical oceans, *J. Clim.*, *22*, 4182–4196.
Batstone, C. P., A. J. Matthews, and D. P. Stevens (2005), Coupled ocean–atmosphere interactions between the Madden–Julian oscillation and synoptic-scale variability over the Warm Pool, *J. Clim.*, *18*, 2004–2020.
Bellenger, H., and J.-P. Duvel (2009), An analysis of tropical ocean diurnal warm layers, *J. Clim.*, *22*, 3629–3646.
Bellenger, H., Y. N. Takayabu, T. Ushiyama, and K. Yoneyama (2010), Role of diurnal warm layers in the diurnal cycle of convection over the tropical Indian ocean during MISMO, *Mon. Weather Rev.*, *138*(6), 2426–2433, doi:10.1175/2010mwr3249.1.
Benedict, J. J., and D. A. Randall (2007), Observed characteristics of the MJO relative to maximum rainfall, *J. Atmos. Sci.*, *64*, 2332–2354.
Benedict, J. J., and D. A. Randall (2009), Structure of the Madden–Julian oscillation in the superparameterized CAM, *J. Clim.*, *66*, 3277–3296.
Benedict, J. J., and D. A. Randall (2011), Impacts of idealized air–sea coupling on Madden–Julian oscillation structure in the superparameterized CAM, *J. Atmos. Sci.*, *68*, 1990–2008.
Betts, A. K. (1986), A new convection adjustment scheme. Part I: Observational and theoretical basis, *Q. J. R. Meteorol. Soc.*, *112*, 677–691.
Bladé, I., and D. L. Hartmann (1993), Tropical intraseasonal oscillations in a simple nonlinear model, *J. Atmos. Sci.*, *50*, 2922–2939.
Bretherton, C. S., M. E. Peters, and L. E. Back (2004), Relationships between water vapor path and precipitation over the tropical oceans, *J. Clim.*, *17*(7), 1517–1528.
Brown, P. J., and C. D. Kummerow (2014), An assessment of atmospheric water budget components over tropical oceans, *J. Clim.*, *27*(5), 2054–2071.
Brunke, M. A., Z. Wang, X. Zeng, M. Bosilovich, and C.-L. Shie (2011), An assessment of the uncertainties in ocean surface turbulent fluxes in 11 reanalysis, satellite-derived and combined global datasets, *J. Clim.*, *24*, 5469–5493.
Chaudhuri, A. H., R. M. Ponte, G. Forget, and P. Heimbach (2013), A comparison of atmospheric reanalysis surface products over the ocean and implications for uncertainties in air–sea boundary forcing, *J. Clim.*, *26*(1), 153–170.
Chikira, M. (2014), Eastward-propagating intraseasonal oscillation represented by Chikira–Sugiyama cumulus parameterization. Part II: Understanding moisture variation under weak temperature gradient balance, *J. Atmos. Sci.*, *71*, 615–639.
Crueger, T., and B. Stevens (2015), The effect of atmospheric radiative heating by clouds on the Madden-Julian oscillation, *J. Adv. Model. Earth Syst.*, *7*, 854–864, doi:10.1002/2015MS000434.
de Boyer Montégut, C., G. Madec, A. S. Fischer, A. Lazar, and D. Iudicone (2004), Mixed layer depth over the global ocean: An examination of profile data and a profile-based climatology, *J. Geophys. Res.*, *109*, C12003, doi:10.1029/2004JC002378.
de Szoeke, S. P., J. B. Edson, J. R. Marion, C. W. Fairall, and L. Bariteau (2015), The MJO and air–sea interaction in TOGA COARE and DYNAMO, *J. Clim.*, *28*, 597–622.

Dee, D. P., et al. (2011), The ERA-Interim reanalysis: Configuration and performance of the data assimilation system, *Q. J. R. Meteorol. Soc.*, *137*, 553–597.

Del Genio, A. D., and Y. Chen (2015), Cloud-radiative driving of the Madden-Julian oscillation as seen by the A-Train, *J. Geophys. Res. Atmos.*, *120*, 5344–5356, doi:10.1002/2015JD023278.

DeMott, C. A., C. Stan, D. A. Randall, and M. D. Branson (2014), Intraseasonal variability in Coupled GCMs: The roles of ocean feedbacks and model physics, *J. Clim.*, *27*(13), 4970–4995, doi:10.1175/jcli-d-13-00760.1.

DeMott, C. A., N. P. Klingaman, and S. J. Woolnough (2015), Atmosphere-ocean coupled processes in the Madden–Julian oscillation, *Rev. Geophys.*, *53*, 1099–1154, doi:10.1002/2014RG000478.

Dias, J., S. Leroux, S. N. Tulich, and G. N. Kiladis (2013), How systematic is organized tropical convection within the MJO?, *Geophys. Res. Lett.*, *40*, 1420–1425, doi:10.1002/grl.50308.

Drushka, K., J. Sprintall, and S. T. Gille (2012), In situ observations of Madden–Julian oscillation mixed layer dynamics in the Indian and western Pacific Oceans, *J. Clim.*, *25*, 2306–2328.

Duvel, J. P., and J. Vialard (2007), Indo-Pacific sea surface temperature perturbations associated with intraseasonal oscillations of tropical convection, *J. Clim.*, *20*(13), 3056–3082, doi:10.1175/jcli4144.1.

Duvel, J. P., R. Roca, and J. Vialard (2004), Ocean mixed layer temperature variations induced by intraseasonal convective perturbations over the Indian Ocean, *J. Atmos. Sci.*, *61*, 1004–1022.

Emanuel, K. A. (1987), An air–sea interaction model of intraseasonal oscillations in the tropics, *J. Atmos. Sci.*, *44*, 2324–2340.

Fairall, C. W., E. F. Bradley, J. S. Godfrey, G. A. Wick, J. B. Edson, and G. S. Young (1996), Cool-skin and warm-layer effects on sea surface temperature, *J. Geophys. Res.*, *101*, 1295–1308.

Fu, X., W. Wang, J.-Y. Lee, B. Wang, K. Kikuchi, J. Xu, J. Li, and S. Weaver (2015), Distinctive roles of air–sea coupling on different MJO events: A new perspective revealed from the DYNAMO/CINDY field campaign, *Mon. Weather Rev.*, *143*(3), 794–812.

Fuchs, Z., and D. J. Raymond (2005), Large-scale modes in a rotating atmosphere with radiative–convective instability and WISHE, *J. Atmos. Sci.*, *62*, 4084–4094.

Gill, A. E. (1980), Some simple solutions for heat-induced tropical circulation, *Q. J. R. Meteorol. Soc.*, *106*, 447–462.

Gottschalck, J., P. E. Roundy, C. J. Schreck III, A. Vintzileos, and C. Zhang (2013), Large-scale atmospheric and oceanic conditions during the 2011–12 DYNAMO field campaign, *Mon. Weather Rev.*, *141*(12), 4173–4196.

Halkides, D. J., D. E. Waliser, T. Lee, D. Menemenlis, and B. Guan (2015), Quantifying the processes controlling intraseasonal mixed-layer temperature variability in the tropical Indian Ocean, *J. Geophys. Res. Oceans*, *120*, 692–715, doi:10.1002/2014JC010139.

Harrison, D. E., and G. A. Vecchi (2001), January 1999 Indian Ocean cooling event, *Geophys. Res. Lett.*, *28*(19), 3717–3720.

Hendon, H. H., and J. Glick (1997), Intraseasonal air-sea interaction in the tropical Indian and Pacific Oceans, *J. Clim.*, *10*, 647–661.

Holloway, C. E., and J. D. Neelin (2009), Moisture vertical structure, column water vapor, and tropical deep convection, *J. Atmos. Sci.*, *66*(6), 1665–1683.

Hsu, P.-C., and T. Li (2012), Role of the boundary layer moisture asymmetry in causing the eastward propagation of the Madden–Julian oscillation, *J. Clim.*, *25*, 4914–4931.

Hu, Q., and D. A. Randall (1994), Low-frequency oscillations in radiative-convective systems, *J. Atmos. Sci.*, *51*(8), 1089–1099.

Inness, P. M., and J. M. Slingo (2003), Simulation of the Madden–Julian oscillation in a coupled general circulation model. Part I: Comparison with observations and an atmosphere-only GCM, *J. Clim.*, *16*, 345–364.

Kemball-Cook, S., B. Wang, and X. Fu (2002), Simulation of the ISO in the ECHAM4 model: The impact of coupling with an ocean model, *J. Atmos. Sci.*, *59*, 1433–1453.

Kemball-Cook, S. R., and B. C. Weare (2001), The onset of convection in the Madden-Julian oscillation, *J. Clim.*, *14*(5), 780–793.

Kent, E. C., S. Fangohr, and D. I. Berry (2013), A comparative assessment of monthly mean wind speed products over the global ocean, *Int. J. Climatol.*, *33*(11), 2520–2541.

Kim, D., et al. (2009), Application of MJO simulation diagnostics to climate models, *J. Clim.*, *22*, 6413–6436.

Kim, D., J.-S. Kug, and A. H. Sobel (2014), Propagating versus nonpropagating Madden–Julian oscillation events, *J. Clim.*, *27*, 111–125.

Kim, D., M.-S. Ahn, I.-S. Kang, and A. D. Del Genio (2015), Role of longwave cloud–radiation feedback in the simulation of the Madden–Julian oscillation, *J. Clim.*, *28*(17), 6979–6994.

Kiranmayi, L., and E. D. Maloney (2011), Intraseasonal moist static energy budget in reanalysis data, *J. Geophys. Res.*, *116*, D21117, doi:10.1029/2011JD016031.

Klingaman, N. P., and S. J. Woolnough (2014a), Using a case-study approach to improve the Madden–Julian oscillation in the Hadley Centre model, *Q. J. R. Meteorol. Soc.*, *140*, 2491–2505.

Klingaman, N. P., and S. J. Woolnough (2014b), The role of air–sea coupling in the simulation of the Madden–Julian oscillation in the Hadley Centre model, *Q. J. R. Meteorol. Soc.*, *140*, 2272–2286.

Koch-Larrouy, A., M. Lengaigne, P. Terray, G. Madec, and S. Masson (2011), Tidal mixing in the Indonesian seas and its effect on the tropical climate system, *Clim. Dyn.*, *34*, 891–904.

Krishnamurti, T. N., D. K. Oosterhof, and A. V. Metha (1988), Air–sea interaction on the timescale of 30–50 days, *J. Atmos. Sci.*, *45*, 1304–1322.

Lappen, C.-L., and C. Schumacher (2012), Heating in the tropical atmosphere: What level of detail is critical for accurate MJO simulations in GCMs?, *Clim. Dyn.*, *39*, 2547–2568.

Lappen, C.-L., and C. Schumacher (2014), The role of tilted heating in the evolution of the MJO, *J. Geophys. Res. Atmos.*, *119*, 2966–2989, doi:10.1002/2013JD020638.

Lau, K. M., and L. Peng (1987), Origin of low-frequency (intraseasonal) oscillationsin the tropical atmosphere, Part I: Basic theory, *J. Atmos. Sci.*, *44*, 950–972.

Lau, K.-M., and C.-H. Sui (1997), Mechanisms of short-term sea surface temperature regulation: Observations during TOGA COARE, *J. Clim.*, *10*, 465–472.

Li, Y., and R. E. Carbone (2012), Excitation of rainfall over the tropical Western Pacific, *J. Atmos. Sci.*, *69*, 2983–2994.

Lin, J. L., W. Han, and X. Lin (2008), Observational analysis of the wind-evaporation-SST feedback over the tropical Pacific Ocean, *Atmos. Sci. Lett.*, *9*(4), 231–236.

Lindzen, R. S., and S. Nigam (1987), On the role of the sea surface temperature gradients in forcing low-level winds and convergence in the Tropics, *J. Atmos. Sci.*, *44*, 2440–2458.

Lloyd, I. D., and G. A. Vecchi (2010), Submonthly Indian Ocean cooling events and their interactions with large-scale conditions, *J. Clim.*, *23*, 700–716.

Madden, R. A., and P. R. Julian (1971), Detection of a 40–50 day oscillation in the zonal wind in the tropical Pacific, *J. Atmos. Sci.*, *28*, 702–708.

Madden, R. A., and P. R. Julian (1972), Description of global-scale circulation cells in the tropics with a 40–50 day period, *J. Atmos. Sci.*, *29*, 1109–1123.

Majda, A. J., and S. N. Stechmann (2009), The skeleton of tropical intraseasonal oscillations, *Proc. Natl. Acad. Sci. U. S. A.*, *106*, 8417–8422.

Majda, A. J., and S. N. Stechmann (2011), Nonlinear dynamics and regional variations in the MJO skeleton, *J. Atmos. Sci.*, *68*(12), 3053–3071.

Maloney, E. D. (2009), The moist static energy budget of a composite tropical intraseasonal oscillation in a climate model, *J. Clim.*, *22*, 711–729.

Maloney, E. D., and S. K. Esbensen (2007), Satellite and buoy observations of boreal summer intraseasonal variability in the tropical northeast Pacific, *Mon. Weather Rev.*, *135*(1), 3–19.

Maloney, E. D., and A. H. Sobel (2004), Surface fluxes and ocean coupling in the tropical intraseasonal oscillation, *J. Clim.*, *17*, 4368–4386.

Marshall, A. G., O. Alves, and H. H. Hendon (2008), An enhanced moisture convergence–evaporation mechanism for MJO air–sea interaction, *J. Atmos. Sci.*, *65*, 970–986.

Matthews, A. J., D. B. Baranowski, K. J. Heywood, P. J. Flatau, and S. Schmidtko (2014), The surface diurnal warm layer in the Indian Ocean during CINDY/DYNAMO, *J. Clim.*, *27*(24), 9101–9122.

McPhaden, M. J. (2002), Mixed layer temperature balance on intraseasonal timescales in the equatorial Pacific Ocean, *J. Clim.*, *15*, 2632–2647.

McPhaden, M. J., and G. R. Foltz (2013), Intraseasonal variations in the surface layer heat balance of the central equatorial Indian Ocean: The importance of zonal advection and vertical mixing, *Geophys. Res. Lett.*, *40*, 2737–2741, doi:10.1002/grl.50536.

Moum, J. N., et al. (2013), Air-sea interactions from westerly wind bursts during the November 2011 MJO in the Indian Ocean, *Bull. Am. Meteorol. Soc.*, *95*, 1185–1199, doi:10.1175/bams-d-12-00225.1.

Neelin, J. D., I. M. Held, and K. H. Cook (1987), Evaporation-wind feedback and low-frequency variability in the tropical atmosphere, *J. Atmos. Sci.*, *44*, 2341–2348.

Powell, S. W., and R. A. Houze (2015), Effect of dry large-scale vertical motions on initial MJO convective onset, *J. Geophys. Res. Atmos.*, *120*, 4783–4805, doi:10.1002/2014JD022961.

Raymond, D. J., and X. Zeng (2005), Modelling tropical atmospheric convection in the context of the weak temperature gradient approximation, *Q. J. R. Meteorol. Soc.*, *131*(608), 1301–1320.

Reynolds, R., N. Rayner, T. M. Smith, D. C. Stokes, and W. Wang (2002), An improved in situ and satellite SST analysis for climate, *J. Clim.*, *15*, 1609–1625.

Riley Dellaripa, E., and E. D. Maloney (2015), Analysis of MJO wind-flux feedbacks in the Indian Ocean using RAMA observations, *J. Meteorol. Soc. Jpn.*, *93*, 1–20.

Roundy, P. E. (2012), Observed structure of convectively coupled waves as a function of equivalent depth: Kelvin waves and the Madden-Julian oscillation, *J. Atmos. Sci.*, *69*(7), 2097–2106.

Ruppert, J. H., and R. H. Johnson (2015), Diurnally modulated cumulus moistening in the preonset stage of the Madden–Julian oscillation during DYNAMO, *J. Atmos. Sci.*, *72*, 1622–1647.

Saji, N. H., S.-P. Xie, and C.-Y. Tam (2006), Satellite observations of intense intraseasonal cooling events in the tropical south Indian Ocean, *Geophys. Res. Lett.*, *33*, L14704, doi:10.1029/2006GL026525.

Saxen, T. R., and S. A. Rutledge (1998), Surface fluxes and boundary layer recovery in TOGA COARE: Sensitivity to convective organization, *J. Atmos. Sci.*, *55*, 2763–2781.

Schott, F. A., S.-P. Xie, and J. P. McCreary (2009), Indian ocean circulation and climate variability, *J. Geophys. Res.*, *47*, RG1002, doi:10.1029/2007RG000245.

Seiki, A., M. Katsumata, T. Horii, T. Hasegawa, K. J. Richards, K. Yoneyama, and R. Shirooka (2013), Abrupt cooling associated with the oceanic Rossby wave and lateral advection during CINDY2011, *J. Geophys. Res. Oceans*, *118*, 5523–5535, doi:10.1002/jgrc.20381.

Sherwood, S. C. (1999), Convective precursors and predictability in the tropical western Pacific, *Mon. Weather Rev.*, *127*(12), 2977–2991.

Shinoda, T., and H. H. Hendon (1998), Mixed layer modeling of intraseasonal variability in the tropical western Pacific and Indian Oceans, *J. Clim.*, *11*, 2668–2685.

Shinoda, T., H. H. Hendon, and J. Glick (1998), Intraseaonal variability of surface fluxes and sea surface temperature in the tropical western Pacific and Indian Oceans, *J. Clim.*, *11*, 1685–1702.

Shinoda, T., T. G. Jensen, M. Flatau, and S. Chen (2013), Surface wind and upper–ocean variability associated with the Madden–Julian oscillation simulated by the Coupled Ocean–Atmosphere Mesoscale Prediction System, *Mon. Weather Rev.*, *141*, 2290–2307.

Slingo, J. M., et al. (1996), Intraseasonal oscillations in 15 atmospheric general circulation models: Results from an AMIP diagnotics subproject, *Clim. Dynam.*, *12*, 325–357.

Sobel, A. H., and E. D. Maloney (2013), Moisture modes and eastward propagation of the MJO, *J. Atmos. Sci.*, *70*, 187–192.

Sobel, A. H., J. Nilsson, and L. M. Polvani (2001), The weak temperature gradient approximation and balanced tropical moisture waves, *J. Atmos. Sci.*, *58*(23), 3650–3665.

Sobel, A. H., E. D. Maloney, G. Bellon, and D. M. Frierson (2010), Surface fluxes and tropical intraseasonal variability: A reassessment, *J. Adv. Model. Earth Sys.*, *2*, 2, doi:10.3894/JAMES.2010.2.2.

Sprintall, J., and M. Tomczak (1992), Evidence of the barrier layer in the surface layer of the tropics, *J. Geophys. Res.*, *97*, 7305–7316.

Sprintall, J., A. L. Gordon, A. Koch-Larrouy, T. Lee, J. T. Potemra, K. Pujiana, and S. E. Wijffels (2014), The Indonesian seas and their role in the coupled ocean–climate system, *Nat. Geosci.*, *7*, 487–492.

Sugiyama, M. (2009), The moisture mode in the quasi-equilibrium tropical circulation model. Part I: Analysis based on the weak temperature gradient approximation, *J. Atmos. Sci.*, *66*(6), 1507–1523.

Sui, C.-H., K.-M. Lau, Y. N. Takayabu, and D. A. Short (1997), Diurnal variations in tropical oceanic cumulus convection during TOGA COARE, *J. Atmos. Sci.*, *54*, 639–655.

Thayer-Calder, K., and D. A. Randall (2009), The role of convective moistening in the Madden-Julian oscillation, *J. Atmos. Sci.*, *66*, 3297–3312.

Tian, B., D. E. Waliser, E. J. Fetzer, B. H. Lambrigtsen, Y. L. Yung, and B. Wang (2006), Vertical moist thermodynamic structure and spatial-temporal evolution of the MJO in AIRS observations, *J. Atmos. Sci.*, *63*(10), 2462–2485.

Valdivieso, M., et al. (2015), An assessment of air–sea heat fluxes from ocean and coupled reanalyses, *Clim. Dyn.*, 1–26, doi:10.1007/s00382-015-2843-3.

Vialard, J., A. Jayakumar, C. Gnanaseelan, M. Lengaigne, D. Sengupta, and B. N. Goswami (2012), Processes of 30–90 day sea-surface temperature variability in the northern Indian Ocean during boreal summer, *Clim. Dyn.*, *38*, 1901–1916.

Vinayachandran, P. N., and N. H. Saji (2008), Mechanisms of South Indian Ocean intraseasonal cooling, *Geophys. Res. Lett.*, *35*, L23607, doi:10.1029/2008GL035733.

Wang, B. (1988), Dynamics of tropical low-frequency waves: An analysis of the moist Kelvin wave, *J. Atmos. Sci.*, *45*, 2051–2065.

Wang, B., and H. Rui (1990), Dynamics of the coupled moist Kelvin-Rossby wave on an equatorial beta-plane, *J. Atmos. Sci.*, *47*, 397–413.

Wang, B., and H. Rui (1994), Convective interaction with boundary-layer dynamics in the development of a tropical intraseasonal system, *J. Atmos. Sci.*, *51*, 1386–1400.

Wang, B., and X. Xie (1998), Coupled modes of the warm pool climate system. Part I: The role of air-sea interaction in maintaining Madden–Julian oscillations, *J. Clim.*, *8*, 2116–2135.

Wang, S., A. H. Sobel, F. Zhang, Y. Q. Sun, Y. Yue, and L. Zhou (2015), Regional simulation of the October and November MJO events observed during the CINDY/DYNAMO field campaign at gray zone resolution, *J. Clim.*, *28*(6), 2097–2119.

Wang, W., and K.-H. Seo (2009), The Madden–Julian oscillation in NCEP coupled model simulation, *Terr. Atmos. Oceanic Sci.*, *20*, 713–725.

Webster, P. J., C. A. Clayson, and J. A. Curry (1996), Clouds, radiation, and the diurnal cycle of sea surface temperature in the tropical western Pacific, *J. Clim.*, *9*, 1712–1730.

Weller, R. A., and S. P. Anderson (1996), Surface meteorology and air–sea fluxes in the western equatorial Pacific warm pool during the TOGA coupled ocean-atmosphere response experiment, *J. Clim.*, *9*, 1959–1990.

Wheeler, M., and G. N. Kiladis (1999), Convectively coupled equatorial waves: Analysis of clouds and temperature in the wavenumber-frequency domain, *J. Atmos. Sci*, *56*(3), 374–399.

Wheeler, M. C., and H. H. Hendon (2004), An all–season real–time multivariate MJO index: Development and index for monitoring and prediction, *Mon. Weather Rev.*, *132*, 1917–1932.

Wing, A. A., and K. A. Emanuel (2014), Physical mechanisms controlling self-aggregation of convection in idealized numerical modeling simulations, *J. Adv. Model. Earth Syst.*, *6*, 59–74, doi:10.1002/2013MS000269.

Woolnough, S. J., J. M. Slingo, and B. J. Hoskins (2000), The relationship between convection and sea surface temperatures on intraseasonal timescales, *J. Clim.*, *13*, 2086–2104.

Xie, S.-P., and J. A. Carton (2004), Tropical Atlantic variability: Patterns, mechanisms, and impacts, in *Earth's Climate*, edited by C. Wang, S. P. Xie, and J. A. Carton, pp. 121–142, AGU, Washington, D. C.

Yokoi, S., M. Katsumata, and K. Yoneyama (2014), Variability in surface meteorology and air-sea fluxes due to cumulus convective systems observed during CINDY/DYNAMO, *J. Geophys. Res. Atmos.*, *119*, 2064–2078, doi:10.1002/2013JD020621.

Yoneyama, K., C. Zhang, and C. N. Long (2013), Tracking pulses of the Madden-Julian oscillation, *Bull. Am. Meteorol. Soc.*, *94*, 1871–1891.

Young, G. S., S. M. Perugini, and C. W. Fairall (1995), Convective wakes in the equatorial Pacific during TOGA, *Mon. Weather Rev.*, *123*, 110–123.

Zhang, C. (2013), Madden–Julian oscillation: Bridging weather and climate, *Bull. Am. Meteorol. Soc.*, *94*, 1849–1870.

Zhang, C., and M. J. McPhaden (2000), Intraseasonal surface cooling in the equatorial western Pacific, *J. Clim.*, *13*, 2261–2276.

Zhang, C., M. Dong, S. Gualdi, H. H. Hendon, E. D. Maloney, A. Marshall, K. R. Sperber, and W. Wang (2006), Simulations of the Madden–Julian oscillation in four pairs of coupled and uncoupled global models, *Clim. Dyn.*, *27*, 573–592.

Zhu, H., and H. H. Hendon (2015), Role of large-scale moisture advection for simulation of the MJO with increased entrainment, *Q. J. R. Meteorol. Soc.*, *141*(691), 2127–2136.